A simple open-source method for highly multiplexed imaging of single cells in tissues and tumours

Jia-Ren Lin*[1,2], Benjamin Izar[1,2,3,4]*, Shaolin Mei[1,3],Shu Wang[1], Parin Shah[3] and Peter K Sorger[1,2]

*These authors contributed equally to this work.

[1]Laboratory of Systems Pharmacology
[2]Ludwig Center for Cancer Research at Harvard
Harvard Medical School
200 Longwood Avenue
Boston, Massachusetts, 02115 USA

[3]Department of Medical Oncology
Dana-Farber Cancer Institute
44 Binney Street, Dana 15
Boston, Massachusetts, 02115 USA

[4]Broad Institute of MIT and Harvard
415 Main Street
Cambridge, Massachusetts, 02139 USA

Pre-publication correspondence should be addressed to Peter K Sorger (peter_sorger@hms.harvard.edu)

copying Chris Bird (Christopher_Bird@hms.harvard.edu)

ABSTRACT

Intratumoural heterogeneity strongly influences the development and progression of cancer as well as responsiveness and resistance to therapy. To improve our ability to measure and analyze such heterogeneity we have developed an open source method for fluorescence imaging of up to 60 protein antigens at subcellular resolution using formalin-fixed, paraffin-embedded (FFPE) tissue samples mounted on glass slides, the most widely used specimens for the diagnosis of cancer and other diseases. As described here, tissue-based cyclic immunofluorescence (t-CyCIF) creates high-dimensional imaging data through successive acquisition of four-color images and requires no specialized instruments or reagents. We apply t-CyCIF to 14 cancer and healthy tissue types and quantify the extent of cell to cell variability in signal transduction cascades, tumor antigens and stromal markers. By imaging immune cell lineage markers we enumerate classes of tumour-infiltrating lymphocytes (TILs) and their spatial relationships to the tumor microenvironment (TME). The simplicity and adaptability of t-CyCIF makes it a powerful method for pre-clinical and clinical research and a natural complement to single-cell genomics.

INTRODUCTION

Advances in DNA and RNA profiling have dramatically improved our understanding of oncogenesis and propelled the development of targeted anti-cancer drugs[1]. Sequence data are particularly useful when an oncogenic driver is both a drug target and a biomarker of drug response, $BRAF^{V600E}$ in melanoma[2] or BCR-ABL[3] in chronic myelogenous leukemia, for example. However, in the case of drugs that act through cell non-autonomous mechanisms, such as immune checkpoint inhibitors (ICIs), tumour-drug interactions must be studied in the context of a multi-cellular environment that includes both cancer and non-malignant stromal and infiltrating immune cells. Multiple studies have established that these aspects of the tumor microenvironment strongly influence the initiation, progression and metastasis of cancer[4] and the magnitude of responsiveness or resistance to therapy[5].

Single cell transcript profiling provides a means to dissect the tumour ecosystems and quantify cell types and states[6]. However, single-cell sequencing usually requires disaggregation of tissues, resulting in loss of spatial context[6,7]. Tissue imaging preserves this context but as currently performed, has relatively low dimensionality, particularly in the case of slides carrying formalin-fixed, paraffin-embedded (FFPE) tissue slices. These are among the most commonly acquired clinical samples and are routinely used to diagnose disease following staining with Haemotoxylin and Eosin (H&E). The potential for immunohistochemistry (IHC) of such samples to aid in diagnosis and prioritization of therapy is well established[8] but IHC is primarily a single channel method: imaging multiple antigens typically involves sequential tissue slices or harsh stripping protocols (although limited multiplexing is possible using IHC and bright-field imaging[9]). Antibody detection by formation of a brown diamino-benzidine (DAB) or similar precipitate is also less quantitative than fluorescence[10]. The limitations of IHC are particularly acute in immuno-oncology[11] in which it is necessary to quantify multiple immune cell types (regulatory and cytotoxic T cells for example) in parallel with expression of multiple tumor antigens and immune checkpoints, such as PD-1/PD-L1 and CTLA-4.

A variety of multiplexed approaches to analyzing tissues that do not involve conventional microscopy have been developed with the goal of simultaneously assaying cell identity, state, and morphology[12–16]. For example, FISSEQ[17] enables genome-scale RNA profiling of tissues at single-cell resolution and multiplexed ion beam imaging (MIBI) and imaging mass cytometry achieve a high degree of multiplexing and excellent signal to noise ratios using metals as labels and mass spectrometry as a detection modality[12,18]. Despite the potential of these new methods, they require specialized instrumentation and reagents, one reason that the great majority of translational and clinical studies still rely on H&E or single-channel IHC staining. There remains a substantial need for highly multiplexed methods that (i) minimize the requirement for specialized instruments and costly, proprietary reagents, (ii) work with conventionally prepared FFPE tissue samples (iii) enable imaging of 20-60 antigens at subcellular resolution across a wide range of cell and tumour types (iv) collect data with sufficient

throughput that large specimens (several square centimeters) can be imaged and analyzed (v) generate high resolution data typical of optical microscopy and (vi) allow investigators to customize the antibody mix to specific questions or tissue types. Among these requirements the last is particularly critical: at the current, early stage of development of high dimensional histology, it is essential that pathologists be able to test the widest possible range of antibodies and antigens in search of those with the greatest diagnostic and predictive value.

This paper describes an open-source method for highly multiplexed fluorescence imaging of tissues, tissue-based cyclic immunofluorescence (t-CyCIF), that significantly extends a method we previously described for tissue culture cells[19]. t-CyCIF assembles images of FFPE tissue slices stained with up to 60 different fluorescent antibodies via successive rounds of 4-channel imaging. t-CyCIF uses widely available reagents, conventional slide scanners, automated slide processors and freely available protocols to create a method that is easy to implement in any research or clinical laboratory. We believe that high dimensional imaging methods by t-CyCIF will become a powerful complement to single cell genomics, enabling routine analysis of the phenotypic geography of cancer at single-cell resolution.

RESULTS

t-CyCIF enables multiplexed imaging of FFPE tissue and tumor specimens at sub-cellular resolution.

In t-CyCIF, multiplexing is achieved using an iterative process (a cycle) performed on a slice cut from a block of FFPE tissue. We have developed t-CyCIF staining conditions for antibodies targeting ~140 different proteins including immune lineage makers, signaling proteins and phosphorylated kinases and transcription factors (some of which are drug targets), markers of cell state including cell cycle stage, quiescence and apoptosis etc. (Table 1). In the implementation described here, each cycle involves four sequential steps (Figure 1A): (i) staining with fluorophore-conjugated antibodies against different protein antigens; we currently use antibodies conjugated to Alexa 488, 555 and 647 (ii) staining

with Hoechst 33342 to mark nuclei (iii) four-channel imaging at low and high magnification (10X and 40X objectives) (iv) fluorophore oxidation using hydrogen peroxide, high pH and UV light followed by a wash step. To reduce the level of auto-fluorescence and minimize non-specific staining, we perform a pre-staining cycle prior to any incubation with primary antibodies (Figure S1A); pre-staining involves incubation with secondary antibodies alone followed by fluorophore oxidation (Figure 1B, Figure S1B-D). The current protocol has been optimized for samples prepared in the standard manner for pathologic diagnosis of cancer (4-5 μm thick FFPE slices mounted on a glass slide). We find that incubation in oxidation solution for 15 min is often adequate for Alexa 555 and 647 conjugated antibodies but reduction of Alexa 488 fluorescence to background levels typically requires 60 min (Figure 1C-E, Figure S1E-G); we routinely perform 60-minute oxidation reactions.

Virtually all tissue samples we have examined can be successfully subjected to 8-20 t-CyCIF cycles, yielding data on the spatial distributions of 24-60 different antigens plus nuclear morphology. The primary requirement appears to be good cellularity: samples in which cells are very sparse tend to be too fragile for repeated imaging, We achieve subcellular resolution using a fluorescence slide scanner (in our studies a RareCyte CyteFinder with 10X 0.3 NA objective and field of view of 1.6 x1.4 mm and a 40X 0.6 NA objective and field of view of 0.42 x 0.35 mm). Immunogenicity does not fall appreciably with cycle number (Figure 1F-G) and the signal-to-noise ratio can actually increase due to a reduction in auto-fluorescence as cycle number increases (Figure S1H-J)[20]. The primary limitation in the number of cycles is tissue integrity: some tissues are physically more robust and can undergo more staining and washing procedures than others (Figure 1H). To date the highest cycle number has been obtained with normal tonsil and skin and with glioblastoma multiforme (GBM), pancreatic cancer and melanoma (Figure S2 and S3). Cell morphology is preserved through multiple cycles: for example, in a t-CyCIF image of tonsil tissue (Figure 2A, Table S1), we can distinguish membrane staining of anti-CD3 and CD8 in Cycle 2, and staining of the nuclear lamina, and nuclear exclusion of NF-κB in Cycle 6 (Figure 2B).

Multiplexed immunofluorescence enables high resolution imaging of large samples. Figure 3 shows a ~2 x 1.5 cm pancreatic ductal adenocarcinoma (PDAC) subjected to 8 rounds of t-CyCIF (Figure 3A, Table S2). The image comprises ~140 10X fields stitched together to reconstruct the full specimen. Differences in subcellular distribution are evident for many markers, but for simplicity, in this paper we only analyze intensity values integrated over a whole cell. Images were segmented using a conventional watershed algorithm and total fluorescent signal was calculated for each cell and antibody stain (Figure 3B-C; see Online Methods for a discussion of caveats). This yielded ~1.5 x 10^5 single cells each with 25 intensity values. When we analyzed the levels of pERK$^{T202/Y204}$ (henceforth pERK, the phosphorylated, active form of the kinase) on a cell by cell basis we found that they were highly correlated with the levels of an activating phosphorylation of the downstream kinase pS6$^{S235/S236}$ (r = 0.81). Similarly, β-catenin levels (a measure of canonical WNT pathway signaling) were highly correlated with E-cadherin and Keratin levels, whereas Vimentin and VEGFR2 receptor levels were anti-correlated (Figure 3D), recapitulating the known dichotomy between epithelial and mesenchymal cell states in normal and diseased tissues

The WNT pathway is frequently activated in PDAC and is important for tumourigenesis of multiple gastrointestinal tumours[21]. Approximately 90% of sporadic PDACs also harbor driver mutations in KRAS, activating the MAPK pathway and promoting tumourigenesis[22]. Studies comparing these pathways have come to different conclusions with respect to their relationship: some studies show concordant activation of MAPK and WNT signaling and others argue for exclusive activation of one pathway or the other[23]. Using t-Stochastic Neighbor Embedding (t-SNE), which clusters cells in 2D based on their proximity in the 25-dimensional space of image intensity data, we identified multiple sub-populations within the same tumor sample representing negative, positive or no correlation between pERK and β-catenin levels (marked with labels "a", 'b" or "c", respectively in Figure 3E). In PDACs malignant cells can be distinguished from stromal cells, to a first approximation, by high proliferative index, which we assessed by we measured by staining for Ki-67 and PCNA[24]. When we gated for cells

that were both Ki67^{high} and PCNA^{high} cells and thus likely to be malignant, we again failed to find a fixed relationship between pERK and β-catenin levels. While we cannot exclude the possibility of phospho-epitope loss during sample preparation, it appears that the full range of possible relationships between the MAPK and WNT signaling pathways described in the literature can be found within a tumor from a single patient. This illustrates the impact of tumor heterogeneity on the activities of key signal transduction pathways.

Multiplex imaging of tumour architecture and immune infiltrates

Immuno-oncology drugs, including ICIs that target CTLA-4 and PD-1/PD-L1 are rapidly changing the therapeutic possibilities for traditionally difficult-to-treat cancers, such melanoma, renal and lung cancers, but responses are still highly variable across and within cancer types. Expression of PD-L1 correlates with responsiveness to ICIs such as pembrolizumab and nivolumab[25] but the negative predictive value of PD-L1 alone is insufficient to stratify patient populations[26]. Imaging for multiple markers such as PD-1, PD-L1, CD4 and CD8 using IHC on sequentially cut tumour slices appears to represent a superior approach to identifying ICI-responsive metastatic melanomas[5]. As a first step in developing multiplexed CyCIF immune biomarkers we developed staining conditions for antibodies against CD45, CD3, CD8, CD45RO, FOXP3, PD-1 and PD-L1 (Table 1). In a typical FFPE section from clear-cell renal cell carcinoma (Figure 3F) we could distinguish a domain rich in non-malignant stroma, which stained strongly for the alpha isoform of smooth muscle actin (α-SMA) and one enriched in tumour cells and low in α-SMA. To examine the spatial distribution of cytotoxic CD8+ T cells within this tumor we stained for several immune markers, including CD8 (Figure 3G), CD3, PD-1 and PD-L1. CD3^{+} CD8^{+} TILs were 4-fold enriched in the tumour-domain (Figure 3H). The subset of CD3^{+} CD8^{+} PD-1^{+} cells that represents a population of putatively exhausted T cells was 18-fold enriched in the tumor-domain (Figure 3H). Moreover, PD-1 and PD-L1 positive cells were 13 to 20-fold more prevalent in the tumour-rich domain (yellow bars, α-SMA low domain) as compared to the tumor stroma (blue bars, α-SMA high domain). Together, these data suggest that PD-1/PD-L1 interactions occur

predominantly within tumour rich domains of kidney cancer and show the potential of t-CyCIF to quantify key features of TILs in combination with their positions in a tumour. Showing that such features constitute true biomarkers will, of course, required additional validation with clinical cohorts.

Analysis of diverse tumour types and grades using CyCIF of tissue-microarrays (TMA)

Tissue microarrays (TMAs) provide a means to analyze a large number of tissues and tumour samples simultaneously, and are frequently used to study patient biopsies collected in clinical trials. We applied 8 cycle t-CyCIF to TMAs containing 39 individual biopsies from 13 healthy tissues as well as low and high-grade tumours for 13 type of cancer (Figure 4A, Figure S4, Table S2 for antibodies used, Table S3 for TMA details and naming conventions) and then performed t-SNE on single cell intensity data (Figure 4B). The great majority of TMA samples mapped to one or a few discrete locations in the t-SNE projection (compare normal kidney tissue - KI1, low grade tumours - KI2, and high grade tumours – KI3; Figure 4C), while other tumours, such as ovarian cancer, showed a scattered pattern in the t-SNE projection (Figure 4D). Overall, there was no separation between normal tissue and tumours regardless of grade (Figure 4E). In a number of cases, high grade cancers from multiple different tissues of origin co-clustered, implying that transformed morphologies and cell states were closely related. For example, while healthy and low grade pancreatic and stomach cancer occupied distinct t-SNE domains, high grade pancreatic and stomach cancers were intermingled and could not be readily distinguished (Figure 4F), recapitulating the known difficulty in distinguishing high grade gastrointestinal tumours of diverse origin by histophathology.[27] Nonetheless, t-CyCIF might represent a means to identify discriminating biomarkers by efficiently sorting through large numbers of alternative antigens, particularly those informed by known genetic features of each disease. Overall we conclude that t-CyCIF can be used on a wide range of normal tissues and tumor types to quantify inter- and intra-tumour heterogeneity.

Quantitative analysis reveals global and regional heterogeneity and multiple histologic subtypes within the same tumour in glioblastoma multiforme (GBM).

Data from single-cell genomics has revealed the extent of intra-tumour heterogeneity[28] but our understanding of this phenomenon would benefit greatly from spatially-resolved data[12]. To study this using t-CyCIF we performed 8 cycle imaging on glioblastoma multiforme, a highly aggressive and genetically heterogeneous[29] brain cancer that is classified into four histologic subtypes[30]. We imaged a 2.5 cm x 1.8 mm resected tumor sample for markers of neural development, cell cycle state and signal transduction state (Figure 5A-B, Table S5). Phenotypic heterogeneity at the level of single tumor cells was assessed at three spatial scales corresponding to: (i) 1.6 x 1.4 mm fields of view (252 total) each of which comprised 10^3 to 10^4 cells (ii) seven macroscopic regions of ~10^4 to 10^5 cells each, corresponding roughly to tumour lobes and (iii) the whole tumour comprising ~10^6 cells. To quantify local heterogeneity we computed the informational entropy on a-per-channel basis for 10^3 randomly selected cells in each field (Figure 5C, see online Methods for details). In this setting, informational entropy is a measure of cell-to-cell heterogeneity on a mesoscale corresponding to 10-30 cell diameters. For a marker such as EGFR, which is a driving oncogene in GBM, informational entropy was high in some areas (Figure 5C; red dots) and low in others (blue dots). Areas with high entropy in EGFR abundance did not co-correlate with areas that were most variable with respect to a downstream signaling protein such as pERK. Thus, the extent of local heterogeneity varied with the region of the tumor and the marker being assayed.

Unsupervised clustering using expectation–maximization Gaussian mixture (EMGM) modeling on all cells in the tumour yielded eight distinct clusters, four of which in aggregate encompassed 85% of the cells (Figure 6A). Among these, cluster one had high EGFR levels, cluster two had high NGFR and Ki67 levels and cluster six had high levels of vimentin; cluster five was characterized by high keratin and pERK levels. The presence of four highly populated t-CyCIF clusters is consistent with data from single-cell RNA-sequencing of ~400 cells from five GBMs[7]. Three of the t-CyCIF clusters have properties reminiscent of classical (cluster 1), pro-neural (cluster 2) and mesenchymal (cluster 6) histological subtypes, but additional work will be required to confirm such assignments. To study the

relationship between phenotypic diversity and tumor architecture, we mapped each cell to an EMGM cluster (denoted by color). Extensive intermixing was observed at the level of fields of view and overall tumor domains (Figure 6B). For example, field of view 147 was highly enriched for cells corresponding to cluster 5 (yellow), but a higher-magnification view revealed extensive intermixing of four other cluster types on a scale of ~3-5 cell diameters (Figure 6C). At the level of larger, macroscopic regions, the fraction of cells from each cluster also varied dramatically (Figure 6D, Figure S5). These findings have several implications. First, they suggest that GBM is a phenotypically heterogeneous on a spatial scale of 5-1000 cell diameters and that cells corresponding to distinct t-CyCIF clusters are often found in the vicinity of each other. Second, sampling a small region of a large tumour has the potential to substantially misrepresent the proportion and distribution of tumour subtypes, with implications for prognosis and therapy. Similar concepts likely apply to other tumor types with high genetic heterogeneity, such as metastatic melanoma, as recently indicated by single-cell genomic analyses[6], and are therefore relevant to diagnostic and therapeutic challenges arising from tumor heterogeneity.

DISCUSSION.

The spatial heterogeneity of solid tumours poses a scientific, diagnostic and therapeutic challenge that is not sufficiently addressed using current methods. We have developed a simple, public-domain approach for quantitative assessment of 20-60 protein antigens in ~5-10μm thick FFPE tissue slices, which represent the norm for diagnosis of human disease and study of mouse models. We describe several applications of t-CyCIF in studying oncogenic signaling, tumour heterogeneity and immune cell-tumour interaction, none of which requires specialized equipment (beyond a slide scanner) or proprietary reagents. t-CyCIF is not as technically sophisticated as FISSEQ[17], MIBI[18] or tissue-based mass cytometry[12], but we regard simplicity as a primary virtue: we have taught t-CyCIF to several other research groups and are confident that it can be readily adopted by many clinical and translational research laboratories. Cyclic immunofluorescence also appears to be substantially higher in throughput

than non-optical methods, particularly when multiple slides are processed in parallel, and considerable opportunity exists for further improvement, for example, by switching from four to six channel imaging per cycle. Good linearity and resolution (~ 400 nm laterally in the current work, but potentially better with higher NA optics or super-resolution microscopes) are additional advantages of direct fluorescence imaging as compared to methods that rely on enzymatic amplification, laser ablation or mechanical picking of tissues. However, some signals, particularly those associated with phospho-epitopes can be very dim and amplification or use of very bright fluorophores such as quantum dots will be required to image them. We therefore continue to optimize t-CyCIF and will make updates available via our website.

In an initial test of t-CyCIF we quantified the relationship between WNT and MAPK-signaling in PDAC. Prior studies performed on tumours or on populations of cells under different conditions have reported conflicting results as to whether or not WNT signaling positively regulates MAPK signaling[31]. Our analysis of PDAC suggests that the activities of the WNT and MAPK signaling cascades can by uncorrelated, positively correlated or negatively correlated within different regions of a single tumor. Thus, what appears to be a set of conflicting findings most likely represents heterogeneity arising from differences in microenvironment, genotype or both. Such data adds new insight into our understanding of disease mechanism but variability may complicated the use of MEK-inhibitors in PDAC.[32]

In a second test of t-CyCIF we studied within-tumor heterogeneity in GBM, a cancer with multiple histological subtypes whose differing properties impact prognosis and therapy.[30,33] Clustering antigen abundance data from t-CyCIF images also reveals multiple phenotypic classes within a single tumor. We have not yet established the link between t-CyCIF clusters and known histological subtypes but our results show that cells with very different characteristics are intermingled at multiple spatial scales with no evidence of recurrent patterns of heterogeneity. In regions of the GBM we have studied in detail, heterogeneity on a scale of 10-100 cell diameters is as great as it is between distinct lobes. The

proportion of cells from different clusters also varies dramatically from one lobe to the next. Variation on this spatial scale is likely to impact the interpretation of small core needle biopsies.

In a third test we characterized tumour-immune cell interactions. Immune checkpoint inhibitors (ICI) produce durable responses in a portion of patients but identifying potential responders and non-responders remains a challenge. Conventional single channel IHC on checkpoint proteins and ligands lacks sufficient positive and negative predictive value to stratify therapy or justify withholding ICIs in favor of small molecule therapy. Multivariate predictors based on multiple markers such as CD3, CD4, CD8, PD-1 etc. are likely to be more effective, but still underperform as patient stratification approaches[5]. This likely arises because cell types other than CD8+ TILs, including malignant, stromal, and myeloid-derived cells affect responses to ICIs. t-CyCIF represents a simple method for simultaneously assessing up to 60 predictors, including several processes and mechanisms, such as angiogenesis regulators, DNA damage, tyrosine kinase expression, proliferation, and others (Figure S3). In the current work, we perform a simple analysis showing that TILs can be subtyped, analyzed for PD-1 levels and proximity to PD-L1 ligand at a single cell level. Next steps include validating more antibodies and developing an efficient means to relate staining patterns to immune cell classes that have been defined primarily by flow cytometry.

Highly multiplexed histology is still in an early stage of development and better methods for segmenting cells, quantifying fluorescence intensities and analyzing the resulting data are required. With better data analysis methods, cell-to-cell heterogeneity in t-CyCIF images should enable reconstruction of signaling network topologies relevant to different regions of a single tumor[12,34] based on the observation that proteins naturally and randomly fluctuate in abundance and activity from one cell to the next. When these fluctuations are highly correlated, they are likely to reflect causal associations[35]. Additional work will also be required to determine which types of heterogeneity are most significant for therapeutic response and disease progression: some cell-to-cell differences observed by fixed cell imaging arise from time-dependent fluctuation. However, we have observe cell-to-cell heterogeneity not

only among proteins known to change over the course of a single cell cycle but also among long-lived proteins. Finally, validation of t-CyCIF-based biomarkers will require extensive testing in patient cohorts. It is important to note in this context that the current study describes a technology and its potential applications to histopathology, not actual diagnostic biomarkers. The associations we describe might not prove statistically significant when tested on larger, well-controlled sets of samples.

In conclusion, the t-CyCIF approach to multi-parametric imaging is robust, simple and applicable to many types of tumours and tissues; as an open platform, it allows investigators to mix and match antibodies depending on the requirements of a specific type of sample. In the long run we expect t-CyCIF to be complementary to, and used in parallel with more sophisticated protein and RNA imaging methods that may have greater sensitivity or channel capacity, although it seems probable that direct imaging will always have better resolution and speed than laser ablation or mechanical picking. A particularly important future development will be cross-referencing tumor cell types identified by single-cell genomics with those identified by multiplexed imaging, making it possible to precisely define the genetic geography of human cancer.

Author contributions.

JR, BI and PKS conceived the study. JR, BI, SM and PS performed experiments. JR, BI, SW and PKS performed analyses. BI, JR and PKS wrote the manuscript.

Competing financial interests

PKS is a member of the Board of Directors of RareCyte Inc., which manufactures the slide scanner used in this study, and co-founder of Glencoe Software, which contributes to and supports open-source OME/OMERO image informatics software. Other authors have no competing financial interests to disclose.

REFERENCES

1. Garraway, L. A. & Lander, E. S. Lessons from the cancer genome. *Cell* **153,** 17–37 (2013).

2. Chapman, P. B. *et al.* Improved Survival with Vemurafenib in Melanoma with BRAF V600E Mutation. *N. Engl. J. Med.* **364,** 2507–2516 (2011).

3. Druker, B. J. & Lydon, N. B. Lessons learned from the development of an Abl tyrosine kinase inhibitor for chronic myelogenous leukemia. *J. Clin. Invest.* **105,** 3–7 (2000).

4. Hanahan, D. & Weinberg, R. A. Hallmarks of cancer: the next generation. *Cell* **144,** 646–674 (2011).

5. Tumeh, P. C. *et al.* PD-1 blockade induces responses by inhibiting adaptive immune resistance. *Nature* **515,** 568–571 (2014).

6. Tirosh, I. *et al.* Dissecting the multicellular ecosystem of metastatic melanoma by single-cell RNA-seq. *Science* **352,** 189–196 (2016).

7. Patel, A. P. *et al.* Single-cell RNA-seq highlights intratumoral heterogeneity in primary glioblastoma. *Science* **344,** 1396–1401 (2014).

8. Bodenmiller, B. Multiplexed Epitope-Based Tissue Imaging for Discovery and Healthcare Applications. *Cell Syst.* **2,** 225–238 (2016).

9. Stack, E. C., Wang, C., Roman, K. A. & Hoyt, C. C. Multiplexed immunohistochemistry, imaging, and quantitation: A review, with an assessment of Tyramide signal amplification, multispectral imaging and multiplex analysis. *Methods* **70,** 46–58 (2014).

10. Rimm, D. L. What brown cannot do for you. *Nat. Biotechnol.* **24,** 914–916 (2006).

11. Postow, M. A., Callahan, M. K. & Wolchok, J. D. Immune Checkpoint Blockade in Cancer Therapy. *J. Clin. Oncol. Off. J. Am. Soc. Clin. Oncol.* **33,** 1974–1982 (2015).

12. Giesen, C. *et al.* Highly multiplexed imaging of tumor tissues with subcellular resolution by mass cytometry. *Nat. Methods* **11,** 417–422 (2014).

13. Gerdes, M. J. *et al.* Highly multiplexed single-cell analysis of formalin-fixed, paraffin-embedded cancer tissue. *Proc. Natl. Acad. Sci. U. S. A.* **110,** 11982–11987 (2013).

14. Micheva, K. D. & Smith, S. J. Array tomography: a new tool for imaging the molecular architecture and ultrastructure of neural circuits. *Neuron* **55,** 25–36 (2007).

15. Remark, R. *et al.* In-depth tissue profiling using multiplexed immunohistochemical consecutive staining on single slide. *Sci. Immunol.* **1,** aaf6925-aaf6925 (2016).

16. Gerner, M. Y., Kastenmuller, W., Ifrim, I., Kabat, J. & Germain, R. N. Histo-cytometry: a method for highly multiplex quantitative tissue imaging analysis applied to dendritic cell subset microanatomy in lymph nodes. *Immunity* **37,** 364–376 (2012).

17. Lee, J. H. *et al.* Highly multiplexed subcellular RNA sequencing in situ. *Science* **343,** 1360–1363 (2014).

18. Angelo, M. *et al.* Multiplexed ion beam imaging of human breast tumors. *Nat. Med.* **20,** 436–442 (2014).

19. Lin, J.-R., Fallahi-Sichani, M. & Sorger, P. K. Highly multiplexed imaging of single cells using a high-throughput cyclic immunofluorescence method. *Nat. Commun.* **6,** 8390 (2015).

20. Lin, J.-R., Fallahi-Sichani, M., Chen, J.-Y. & Sorger, P. K. Cyclic Immunofluorescence (CycIF), A Highly Multiplexed Method for Single-cell Imaging. *Curr. Protoc. Chem. Biol.* **8,** 251–264 (2016).

21. Jones, S. *et al.* Core Signaling Pathways in Human Pancreatic Cancers Revealed by Global Genomic Analyses. *Science* **321,** 1801–1806 (2008).

22. Vogelstein, B. *et al.* Cancer Genome Landscapes. *Science* **339,** 1546–1558 (2013).

23. Jeong, W.-J. *et al.* Ras stabilization through aberrant activation of Wnt/β-catenin signaling promotes intestinal tumorigenesis. *Sci. Signal.* **5,** ra30 (2012).

24. Bologna-Molina, R., Mosqueda-Taylor, A., Molina-Frechero, N., Mori-Estevez, A. D. & Sánchez-Acuña, G. Comparison of the value of PCNA and Ki-67 as markers of cell proliferation in ameloblastic tumor. *Med. Oral Patol. Oral Cir. Bucal* **18,** e174–e179 (2013).

25. Mahoney, K. M. & Atkins, M. B. Prognostic and predictive markers for the new immunotherapies. *Oncol. Williston Park N* **28 Suppl 3,** 39–48 (2014).

26. Sharma, P. & Allison, J. P. The future of immune checkpoint therapy. *Science* **348,** 56–61 (2015).

27. Varadhachary, G. R. & Raber, M. N. Cancer of Unknown Primary Site. *N. Engl. J. Med.* **371,** 757–765 (2014).

28. Turner, N. C. & Reis-Filho, J. S. Genetic heterogeneity and cancer drug resistance. *Lancet Oncol.* **13,** e178–e185 (2012).

29. Brennan, C. W. *et al.* The somatic genomic landscape of glioblastoma. *Cell* **155,** 462–477 (2013).

30. Olar, A. & Aldape, K. D. Using the molecular classification of glioblastoma to inform personalized treatment. *J. Pathol.* **232,** 165–177 (2014).

31. Ilmer, M. *et al.* RSPO2 Enhances Canonical Wnt Signaling to Confer Stemness-Associated Traits to Susceptible Pancreatic Cancer Cells. *Cancer Res.* **75,** 1883–1896 (2015).

32. Zeitouni, D., Pylayeva-Gupta, Y., Der, C. J. & Bryant, K. L. KRAS Mutant Pancreatic Cancer: No Lone Path to an Effective Treatment. *Cancers* **8,** (2016).

33. Phillips, H. S. *et al.* Molecular subclasses of high-grade glioma predict prognosis, delineate a pattern of disease progression, and resemble stages in neurogenesis. *Cancer Cell* **9,** 157–173 (2006).

34. Sachs, K., Gifford, D., Jaakkola, T., Sorger, P. & Lauffenburger, D. A. Bayesian network approach to cell signaling pathway modeling. *Sci. STKE Signal Transduct. Knowl. Environ.* **2002,** pe38 (2002).

35. Vilela, M. & Danuser, G. What's wrong with correlative experiments? *Nat. Cell Biol.* **13,** 1011 (2011).

FIGURE LEGENDS

Figure 1. Steps in the t-CyCIF process and their properties (A) Schematic of the cyclic process whereby t-CyCIF images are assembled via multiple rounds of four-color imaging. **(B)** Image of human tonsil prior to pre-staining and then over the course of three rounds of t-CyCIF. Arrows shows the position of an object that fluoresces in the green channel (use for Alexa-488 imaging) and becomes progressively less intense with cycle number; the phenomenon of decreasing background signal and increasing signal-to-noise ratio as cycle number increases is common. **(C)** Images of tonsil tissue stained with Alexa 488 conjugated to anti-PCNA antibodies and then subjected to fluorophore inactivation conditions (a high pH hydrogen peroxide solution and light) for 0-60 min. **(D)** Distribution of pixel intensities in the sample in panel C. **(E)** Effect of bleaching duration (0-60 minutes) and fluorophore inactivation for tonsil tissue stained with antibodies conjugated to Alexa 488, 570 or 647. **(F)** Impact of cycle number on antigenicity as evaluated using tonsil tissue stained with Alexa 488 conjugated anti-PCNA antibodies. Because primary antibodies remain bound to antigen after fluorophore inactivation, it is not possible to assay the same field repeatedly with the same antibody; thus, different fields are show for each cycle. **(G)** Distribution of single-cell intensities from images in panel (F). Each distribution represents ~2 x 10^4 cells. **(H)** Impact of t-CyCIF cycle number on tissue integrity as measured by the fraction of cells detected in the Hoechst channel in successive cycles; error bars represent the standard error of the mean (S.E.M) for different fields.

Figure 2. Ten-cycle t-CyCIF of human tonsil tissue. (A) A selected image across ten cycles stained with antibodies against the antigens indicated; see Table S1 for a list of antibodies used. **(B)** Images of selected channels and cycles emphasizing sub-cellular features.

Figure 3. Eight-cycle t-CyCIF images of human tumor samples. (A) t-CyCIF image of pancreatic adenocarcinoma. On the left, the entire tumour, comprising 143 stitched 10X fields of view is shown.

On the right, a representative field is shown through all 8 t-CyCIF rounds. **(B)** Representative field at high magnification showing the spatial distribution of PCNA, β-catenin, Ki67 and pERK-positive cells. **(C)** Representation of t-CyCIF image in panel (B) following image segmentation with each dot denoting the centroid of a single cell and the color representing the intensity of a particular antibody stain. **(D)** Quantitative single-cell signal intensities of 24 proteins (rows) measured in ~4 x 10^3 cells (columns) from panel (C). The degree of correlation of each measured protein with E-cadherin (at a single-cell level) is shown numerically; proteins highlighted in red are further analyzed in panel (E). **(E)** t-stochastic neighbor embedding (t-SNE) of cells analyzed in panel (D) with intensity measurements for selected proteins. Circled regions represent t-SNE domains in which the relationship between pERK levels (a measure of MAPK signaling) and β-catenin levels (a measure WNT signaling) are, on average, negatively (a) or positively (b) correlated or uncorrelated (c). **(F)** t-CyCIF of a clear cell renal cancer subjected to 12-cycle t-CyCIF. Regions high in α-smooth muscle actin (α-SMA) correspond to stromal components of the tumors, those low in α-SMA represent regions enriched for malignant cells. **(G)** The same tumor region as in (F) following image segmentation. Each dot denotes the centroid of a single cell. Cells staining positively for α-SMA or the T cell marker CD8 are highlighted in red or green, respectively, and other cells are represented only by nuclear staining (blue). **(H)** Fraction of cells (relative to all cells) with positive staining for immune markers depending on the tumor region (α-SMA high vs. α-SMA low).

Figure 4. Eight-cycle t-CyCIF of a tissue microarray (TMA) including 13 normal and tumor tissue types. The TMA carried 13 normal tissue types, and corresponding high and low grade tumors, for a total of 39 specimens (Table S2-3). **(A)** Selected images of different tissues illustrating the quality of t-CyCIF images (additional examples shown in Figure S3. A full gallery of staining for all samples from this TMA is available online (https://omero.hms.harvard.edu/webclient/?show=dataset-2037

). **(B)** t-SNE plot of single-cell intensity data derived from all 39 samples; data were analyzed using the CYT package (see materials and methods). Tissues of origin and corresponding malignant lesions were labeled as follows: BL, bladder cancer; BR, breast cancer CO, Colorectal adenocarcinoma, KI, clear cell renal cancer, LI, hepatocellular carcinoma, LU, lung adenocarcinoma, LY, lymphoma, OV, high-grade serous adenocarcinoma of the ovary, PA, pancreatic ductal adenocarcinoma, PR, prostate adenocarcinoma, UT, uterine cancer, SK, skin cancer (melanoma), ST, stomach (gastric) cancer. Numbers refer to sample type; "1" to normal tissue, "2" to -grade tumors and "3" to high grade tumors. **(C)** Detail from panel B of normal kidney tissue (KI1) a low-grade tumor (KI2) and a high-grade tumor (KI3) **(D)** Detail from panel B of normal ovary (OV1) low-grade tumor (OV2) and high-grade tumor (OV3). **(E)** t-SNE plot from Panel B coded to show the distributions of all normal, low grade and high grade tumors. **(F)** tSNE clustering of normal pancreas (PA1) and pancreatic cancers (low grade, PA2, and high grade, PA3) and normal stomach (ST1) and gastric cancers (ST2 and ST3, respectively) showing intermingling of high grade tumors.

Figure 5. Molecular heterogeneity in a single GBM tumor. **(A)** Representative low magnification image of a GBM specimen generated from 221 stitched 10X frames; the sample was subjected to 10 rounds of t-CyCIF using antibodies listed in Table S4 **(B)** Magnification of frame 152 (whose position is marked with a white box in panel A) showing staining of pERK, pRB and EGFR; lower panel shows a further 4-fold increase in magnification to allow single cells to be identified. **(C)** Normalized Shannon entropy of each of 221 fields of view to determine the extent of variability in signal intensity for 1000 cells randomly selected from that field for each of the antibodies shown. The size of the circles denotes the number of cells in the field and the color represents the value of the normalized Shannon entropy (data are shown only for those fields having more than 1,000 cells; see Online Methods for details).

Figure 6. Spatial distribution of molecular phenotypes in a single GBM. **(A)** Intensity values from the tumor in Figure 5 were clustered using expected-maximization with Gaussian mixtures (EMGM),

yielding eight clusters, of which four clusters accounted for the majority of cells. The number of cells in each cluster is shown as a percentage of all cells in the tumor. **(B)** EMGM clusters (in color code) mapped back to singles cells and their positions in the tumor. The coordinate system is the same as in Figure 5, Panel A. The positions of seven macroscopic regions (R1-R7) representing distinct lobes of the tumour are also shown. **(C)** Magnified view of Frame 147 from region R5 with EMGM cluster assignment for each cell in the frame shown as a dot. **(D)** The proportional representation of EMGM clusters in each tumor region as defined in panel B.

Table 1. List of antibodies tested and validated for t-CyCIF.

ONLINE METHODS

We continue to improve the methods described here; periodic updates can be found at our web site

http://lincs.hms.harvard.edu/resources/. A video illustrating the t-CyCIF approach can be found at

https://youtu.be/fInnargF2fs.

Patients and specimens

Tumor tissue and FFPE specimens were collected from patients under IRB-approved protocols (DFCI

11-104) at Dana-Farber Cancer Institute/Brigham and Women's Hospital, Boston, Massachusetts. Tonsil

samples were purchased from American MasterTech (CST0224P). Tissue microarrays (TMA) were

obtained from Protein Biotechnologies (TMA-1207).

Reagents and antibodies

All conjugated and unconjugated primary antibodies used in this study are listed in Table 1. Indirect

immunofluorescence was performed using secondary antibodies conjugated with Alexa-647 anti-Mouse

(Invitrogen, Cat. A-21236), Alexa-555 anti-Rat (Invitrogen, Cat. A-21434) and Alexa-488 anti-Rabbit

(Invitrogen, Cat. A-11034). 10 mg/ml Hoechst 33342 stock solution was purchased from Life

Technologies (Cat. H3570). 20x PBS was purchased from Santa Cruz Biotechnology (Cat. SC-362299).

30% hydrogen peroxide solution was purchased from Sigma-Aldrich (Cat. 216763). PBS-based

Odyssey blocking buffer was purchased from LI-COR (Cat. 927-40150). All reagents for the Leica

BOND RX were purchased from Leica Microsystems.

Pre-processing and pre-staining tissues for t-CyCIF

Automated dewaxing, rehydration and pre-staining

Pre-processing of FFPE tissue and tumor slices mounted on slides was performed on a Leica BOND RX

automated stained using the following protocol:

Step	Reagent	Supplier	Incubation (min)	Temp. (^{o}C)
1	*No Reagent	N/D	30	60

2	BOND Dewax Solution	Leica	0	60
3	BOND Dewax Solution	Leica	0	R.T.
4	BOND Dewax Solution	Leica	0	R.T.
5	200 proof ethanol	User*	0	R.T.
6	200 proof ethanol	User*	0	R.T.
7	200 proof ethanol	User*	0	R.T.
8	Bond Wash Solution	Leica	0	R.T.
9	Bond Wash Solution	Leica	0	R.T.
10	Bond Wash Solution	Leica	0	R.T.
11	Bond ER1 solution	Leica	0	99
12	Bond ER1 solution	Leica	0	99
13	Bond ER1 solution	Leica	20	99
14	Bond ER1 solution	Leica	0	R.T.
15	Bond Wash Solution	Leica	0	R.T.
16	Bond Wash Solution	Leica	0	R.T.
17	Bond Wash Solution	Leica	0	R.T.
18	Bond Wash Solution	Leica	0	R.T.
19	Bond Wash Solution	Leica	0	R.T.
20	IF Block	User*	30	R.T.
21	Antibody Mix	User*	60	R.T.
22	Bond Wash Solution	Leica	0	R.T.
23	Bond Wash Solution	Leica	0	R.T.
24	Bond Wash Solution	Leica	0	R.T.
25	Hoechst Solution	User*	30	R.T.
26	Bond Wash Solution	Leica	0	R.T.
27	Bond Wash Solution	Leica	0	R.T.
28	Bond Wash Solution	Leica	0	R.T.

Steps 2-10: Dewaxing & Rehydration with Leica Bond Dewax Solution Cat. AR9222.

Steps 11-14: Antigen retrieval with BOND Epitope Retrieval solution 1 (ER1; Cat. AR9961)

Steps 15-19: Washing with Leica Bond Wash Solution (Cat. AR9590).

Steps 20-28 Pre-staining procedures as shown in Figure S1A:

Step 20: IF Block - Immunofluorescence blocking in Odyssey blocking buffer (LI-COR, Cat. 927401)

Step 21: Antibody Mix - Incubation with secondary antibodies diluted in Odyssey blocking buffer

Step 25: Staining with Hoechst 33342 at 2 μg/ml (w/v) in in Odyssey blocking buffer

Manual dewaxing, rehydration and pre-staining. In our experience dewaxing, rehydration and pre-staining can also be performed manually with similar results. For manual pre-processing, FFPE slides were first incubated in a 60°C oven for 30 minutes. To completely remove paraffin, slides were placed in a glass slide rack were then immediately immersed in Xylene in a glass staining dish (Wheaton 900200) for 5 min and subsequently transferred to a another dish containing fresh Xylene for 5 min. Rehydration was achieved by sequentially immersing slides, for 3 min each, in staining dishes containing 100% ethanol, 90% ethanol, 70% ethanol, 50% ethanol, 30% ethanol, and then in two successive 1xPBS solutions. Following rehydration, slides were placed in a 1000 ml beaker filled with 500 ml citric acid, pH 6.0, for antigen retrieval. The beaker containing slides and citric acid buffer was microwaved at low power until the solution was at a boiling point and maintained at that temperature for 10 min. After cooling to room temperature, slides were washed 3 times with 1xPBS in vertical staining jars followed by blocking with Odyssey blocking buffer. Buffer was applied to slides as a 250-500 μl droplet for 30 mins at room temperature; evaporation was minimized by using moist in a slide moisture chamber (Scientific Device Laboratory, 197-BL). Slides were then pre-stained by incubation with diluted secondary antibodies (listed above) for 60 minutes, followed by washing 3 times with 1x PBS. Finally, slides were incubated with Hoechst 33342 (2 μg/ml) in 250-500 μl Odyssey blocking buffer for 30 min. in a moisture chamber and washed 3 times with 1xPBS in vertical staining jars.

Cyclic immunofluorescence with primary antibodies and Hoechst 33342

All primary antibodies (fluorophore-conjugated and unconjugated) were diluted in Odyssey blocking buffer. Slides carrying dewaxed, pre-stained tissues were then stained in a moisture chamber by dropping the diluted primary or fluorophore-conjugated antibody (250-500 μl per slides) on tissue followed by incubation at 4°C for ~12 hr. Slides were washed four times in 1x PBS by dipping in a series of vertical staining jars. For indirect immunofluorescence, slides were incubated in diluted secondary antibodies in a moisture chamber for 1 hr at room temperature followed by four washes with 1x PBS. Slides were incubated in Hoechst 33342 at 2 μg/ml in Odyssey blocking buffer for 15 min at

room temperature, followed by four washes in 1x PBS. Stained slides were mounted prior to image acquisition (see the Mounting section below).

Primary antibodies

For t-CyCIF, we selected commercial antibodies previously validated by their manufacturers for use in immunofluorescence, immunocytochemistry or immunohistochemistry (IF, ICC or IHC). When possible, we checked antibodies on reference tissue known to express the target antigen, such as immune cells in tonsil tissue or tumor-specific markers in tissue microarrays. The staining patterns for antibodies with favorable signal-to-noise ratios were compared to those previously reported for that antigen by conventional antibodies. An updated list of all antibodies tested to date can be found at the HMS LINCS website (http://lincs.hms.harvard.edu/resources/). The extent of validation is quantified on a level between 0 and 2: "Level 0" represents antibodies for which staining was not detected using tissues for which the antigen is thought to be present based on published data; "Level 1" represents the expected pattern of positive staining in a limited number of tissues types (e.g. CD4 antibody in tonsil tissue alone); "Level 2" represents the expected pattern of positive staining in all tissues or tumor types been tested (N>= 3). Higher levels will be assigned in the future to antibodies that have undergone extensive validation; for example, side-by side comparison of against an established IHC positive control.

Mounting & de-coverslipping

Immediately prior to imaging slides were mounted with 1x PBS or, if imaging was expected to take longer than 30 minutes (this occurs in the case of samples larger than 4 cm^2 corresponding to about 200 fields of view with a 10X objective) with 1x PBS containing 10% Glycerol. Slides were covered using 24 x 60mm No. 1 coverslips (VWR 48393-106) to prevent evaporation and to facilitate susbequent de-coverslipping via gravity. Following image acquisition, slides were placed in a vertical staining jar containing 1x PBS for at least 15 min. Coverslips were released from slides (and the tissue sample) via gravity as the slides were slowly drawn out of the staining jar.

Fluorophore inactivation

After imaging, fluorophores were inactivated by placing slides horizontally in 4.5% H_2O_2 and 24 mM NaOH made up in PBS for 1 hour at RT in the presence of white light. Following fluorophore inactivation, slides were washed 4 times with 1x PBS by dipping them in a series of vertical staining jars to remove residual inactivation solution.

Image acquisition

Stained slides from each round of CycIF were imaged with a CyteFinder slide scanning fluorescence microscope (RareCyte Inc. Seattle WA) using either a 10X (NA=0.3) or 40X long-working distance objective (NA = 0.6). Imager5 software (RareCyte Inc.) was used to sequentially scan the region of interest in 4 fluorescence channels. These channels are referred to by the manufacturer as: (i) a DAPI channel with an excitation filter having a peak of 390 nm and half-width of 18nm and an emission filter with a peak of 435nm and half-width of 48nm; (ii) FITC channel having a 475nm/28nm excitation filter and 525nm/48nm emission filter (iii); Cy3 channel having a 542nm/27nm excitation filter and 597nm/45nm emission filter and (iv); Cy5 channel having a 632nm/22nm excitation filter and 679nm/34nm emission filter. Imaging was performed with a 2x2 binning strategy to increase sensitivity, reducing exposure time and photo bleaching. We have tested slide scanners from several other manufacturers (e.g. a Leica Aperio Digital Pathology Slide Scanner, GE IN-Cell Analyzer 6000 and GE Cytell Cell Imaging System) and found that they too can be used to acquire images from t-CyCIF samples. Slides can also be analyzed on conventional microscopes, but the field of view is typically smaller, and an automated stage is required for accurate stitching of individual fields of view into a complete image of a tissue.

Image processing

Quantitative analysis of tissue images is a complex, in large part because cells are close packed. Background can be uneven across large images and signal to noise ratios relatively low, particularly in the case of anti-phospho-protein antibodies. We have only started to tackle these issues in the case of high dimensional t-CyCIF data and users of the method are encouraged to thoroughly research image

processing methods themselves. We expect to update methods and algorithms described here on a regular basis and users are encouraged to check our Web site for additional information.

Background subtraction and image registration

Background subtraction was performed using the previously established rolling ball algorithm (with a 50-pixel radius) in ImageJ. Adjacent background-subtracted images from the same sample were then registered to each using an ImageJ script as described previously[1]. In brief, DAPI images from each cycle were used to generate reference coordinates by Rigid-body transformation. To generate virtual hyper-stacked images, the transformed coordinates were applied to images from four channel imaging of each CyCIF cycle.

Single-cell segmentation & quantification

To obtain intensity values for single cells, images were segmented using a previously described[2] conventional waterfall algorithm based on nuclear staining by Hoechst 33342. Images were binarized in the Hoechst channel and then converted into regions of interest (ROIs) for each cell. The Watershed algorithm in ImageJ was then applied to enlarge ROIs (by 3 pixels in the case of 10 x images) and encompass a significant portion of the cytoplasm and membrane for each cell. ROIs were then used to compute intensity values from all channels. All scripts can be found in our Github repository (https://github.com/sorgerlab/cycif).

High-dimensional single-cell analysis by t-SNE and EMGM

Raw intensity data generated from registered and segmented images was imported into Matlab and converted to comma separated value (csv) files. The viSNE implementation of t-SNE and EMGM algorithms from the CYT single-cell analysis package were obtained from the Pe'er laboratory at Columbia University[3]. Intensity-based measurements (such as flow cytometry or imaging cytometry) of protein expression have approximately log-normal distribution[4], hence, t-CyCIF raw intensity values were first transformed in log or in inverse hyperbolic sine (*asinh*) using the default Matlab function or the *CYT* package[3], respectively. Between-sample variation was then normalized on a per-channel basis

by aligning intensity measurements that encompass values between 1st and the 99th percentile (using the *CYT* package). Data files were aggregated and used to generate viSNE plots. All viSNE/t-SNE analyses used the following settings: perplexity -30, epsilon =500, lie factor =4 for initial 100 iterations and lie factor -1 for remaining iterations. For EMGM clustering, k = 8 was used for dividing samples into groups. Intensity values from all antibody channels (plus area and Hoechst intensity) were used for unsupervised clustering.

Calculating Shannon entropy values

Images were divided into regular grids and 1000 cells from each region used to calculate the non-parametric Shannon entropy as follows:

$$E1(s) = -\sum_i s_i^2 \log(s_i^2)$$

where E1(s) is the Shannon entropy of signal **s**; s_i is the per-pixel intensity of signal **s** at a given point. Normalized Shannon entropy as calculated as $E_{normalized} = E_{region} / E_{sample}$

Data availability

Intensity data used to generate figures 1D-E, 1G-H, 3D-E, 3G-H, 4B-F, 5C, 6A-6D is available in supplementary materials and can be downloaded from the HMS LINCS website (http://lincs.hms.harvard.edu/lin-tbd-2017/

Code availability

All ImageJ & Matlab scripts used in this study are available at the Sorgerlab GitHub Repo (https://github.com/sorgerlab/cycif).

Image availability

All images can be accessed through HMS LINCS page (http://lincs.hms.harvard.edu/lin-tbd-2017/).

Note that publically available OMERO Web clients do not yet support viewing of very large stitched images and only representative image fields are shown. We are currently working on software that will enable the analysis and distribution of very large images via an OMERO Web client.

Specific image sets can be accessed as follows:

For Tonsil composite images (Figure 2 & Table S1):

> https://omero.hms.harvard.edu/webclient/?show=dataset-2038

For PDAC composite images (Figure 3 & Table S2):

> https://omero.hms.harvard.edu/webclient/?show=dataset-2039

For RCC composite images (Figure 3 & Table S4):

> https://omero.hms.harvard.edu/webclient/?show=dataset-2040

For TMA panels (Figure 3& Table S2/S3):

> https://omero.hms.harvard.edu/webclient/?show=dataset-2037

For GBM composites images (Figure 5, Figure 6 & Table S5)

> https://omero.hms.harvard.edu/webclient/?show=dataset-2041

REFERENCES

1. Lin, J.-R., Fallahi-Sichani, M. & Sorger, P. K. Highly multiplexed imaging of single cells using a high-throughput cyclic immunofluorescence method. *Nat. Commun.* **6,** 8390 (2015).

2. Carpenter, A. E. *et al.* CellProfiler: image analysis software for identifying and quantifying cell phenotypes. *Genome Biol.* **7,** R100 (2006).

3. Amir, E. D. *et al.* viSNE enables visualization of high dimensional single-cell data and reveals phenotypic heterogeneity of leukemia. *Nat. Biotechnol.* **31,** 545–552 (2013).

4. Bagwell, C. B. Hyperlog-a flexible log-like transform for negative, zero, and positive valued data. *Cytom. Part J. Int. Soc. Anal. Cytol.* **64,** 34–42 (2005).

Figure 1
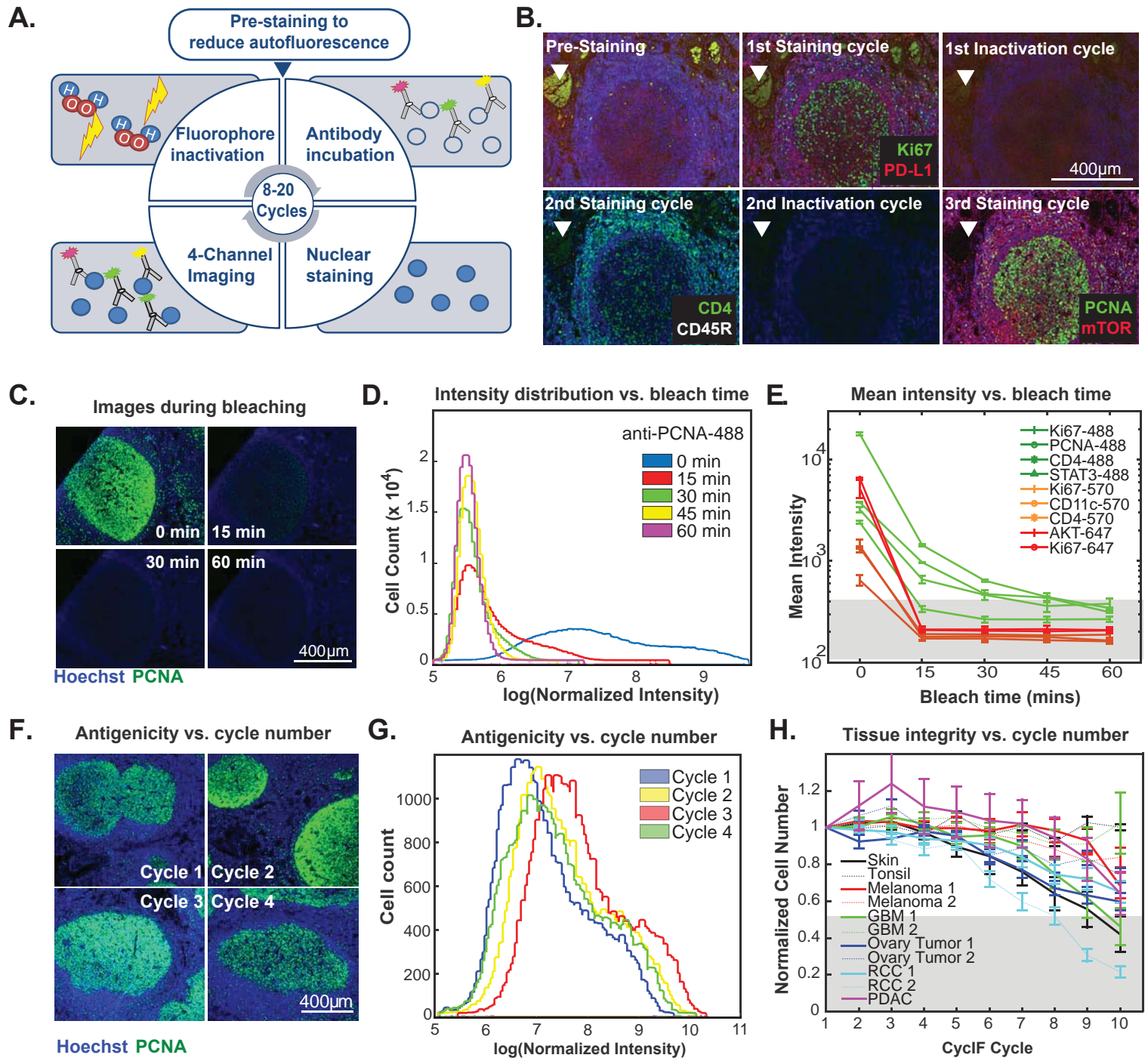
Figure 2
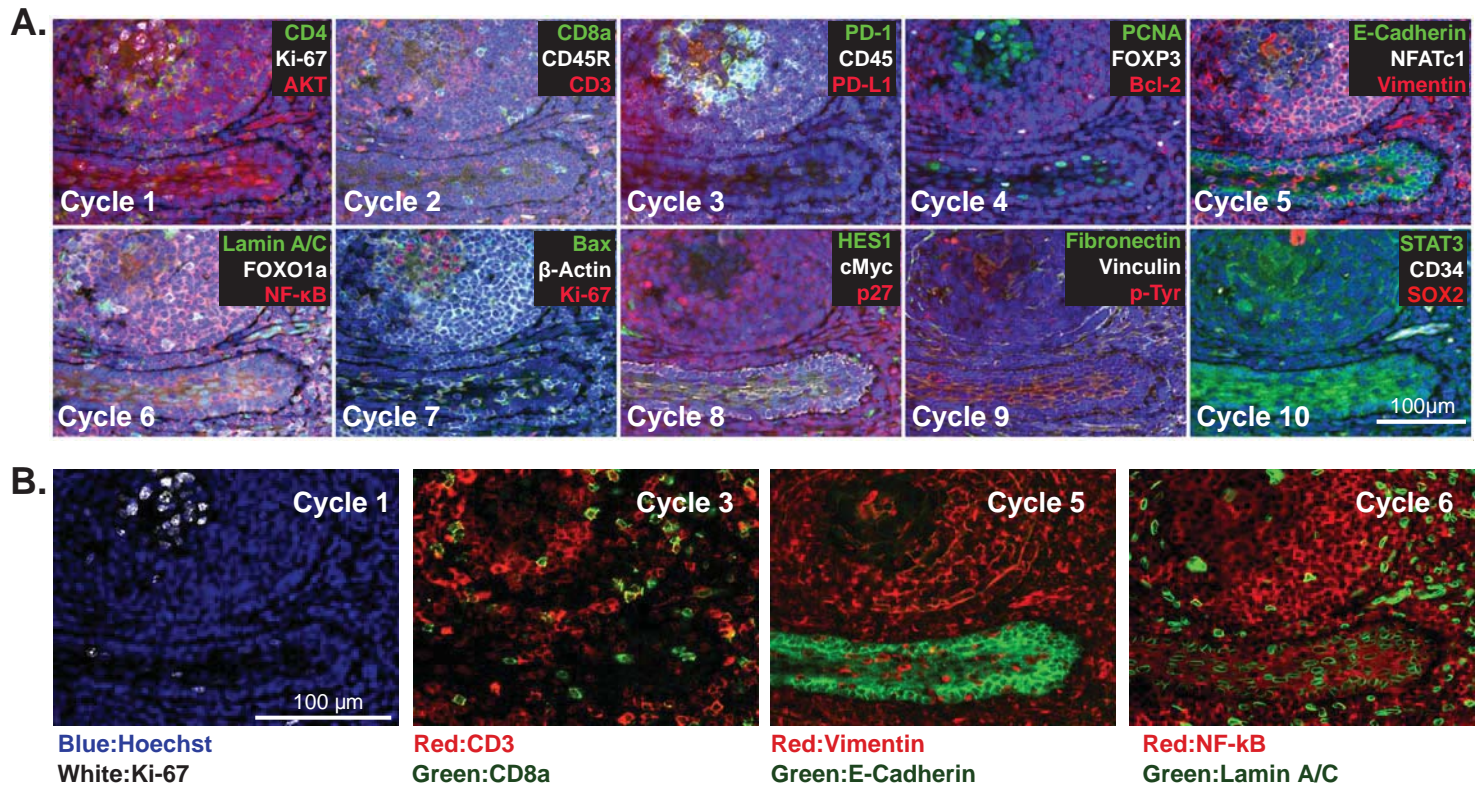
Figure 3
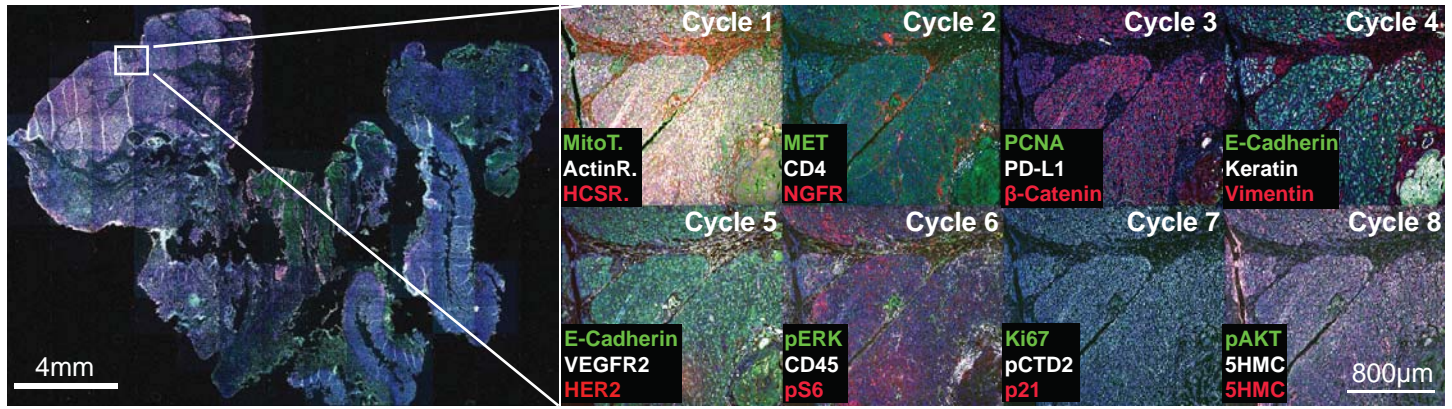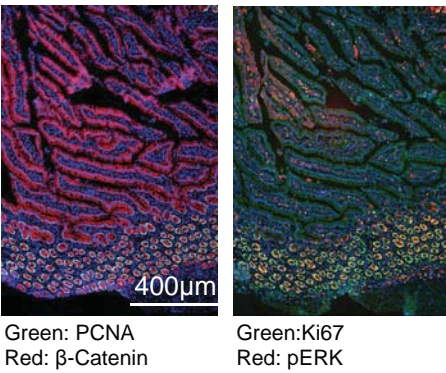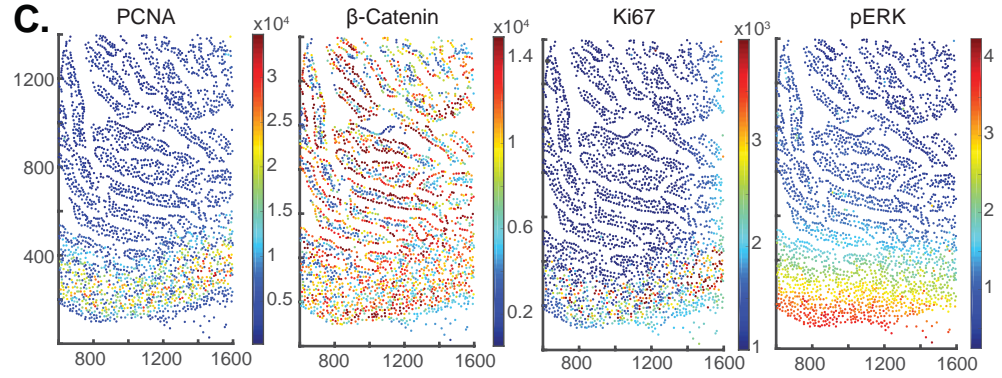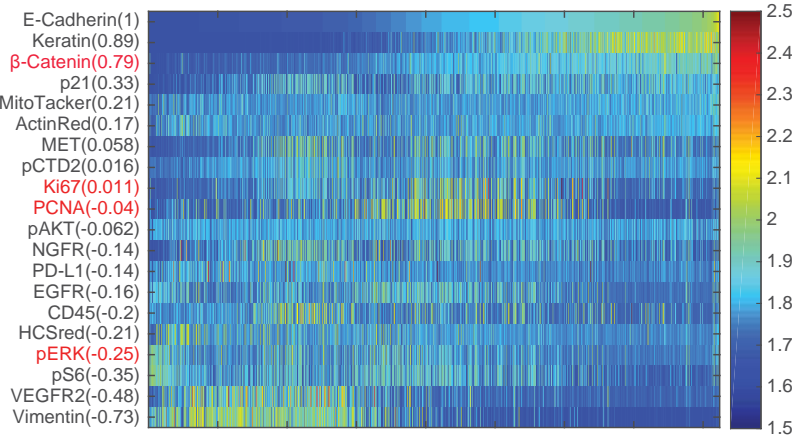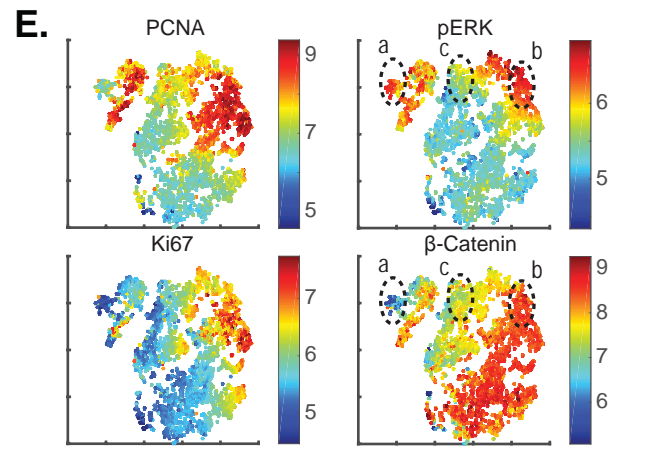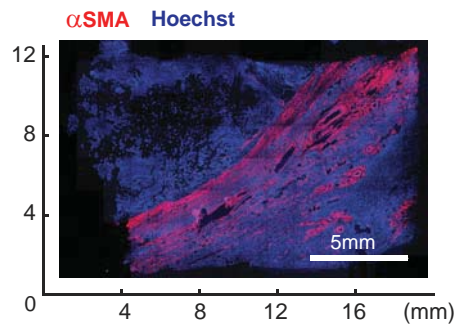
Figure 4

A.

Normal Kidney
E-Cadherin
Vimentin

Breast carcinoma
EGFR
VEGFR2

Lymph node (Reactive)
CD4
NGFR

Melanoma, grade II
PCNA
PD-L1
200µm

B.

All tumours

C.

Kidney

D.

Ovary

E.

● Normal   ● Low grade   ● High grade tumors

F.

PA1-3: Pancreas Tissue; low/high grade PDAC
ST1-3: Stomach; low/high grade gastic cancer

FIGURE 5

Figure 6

A.

B.

C. Frame 147 from Region R5

D.
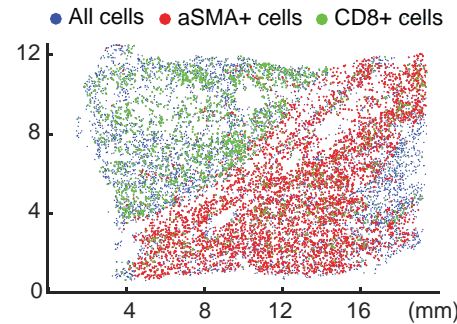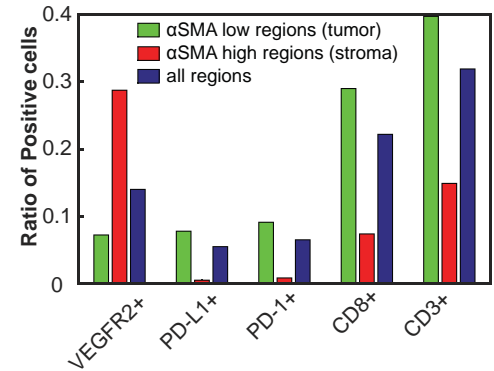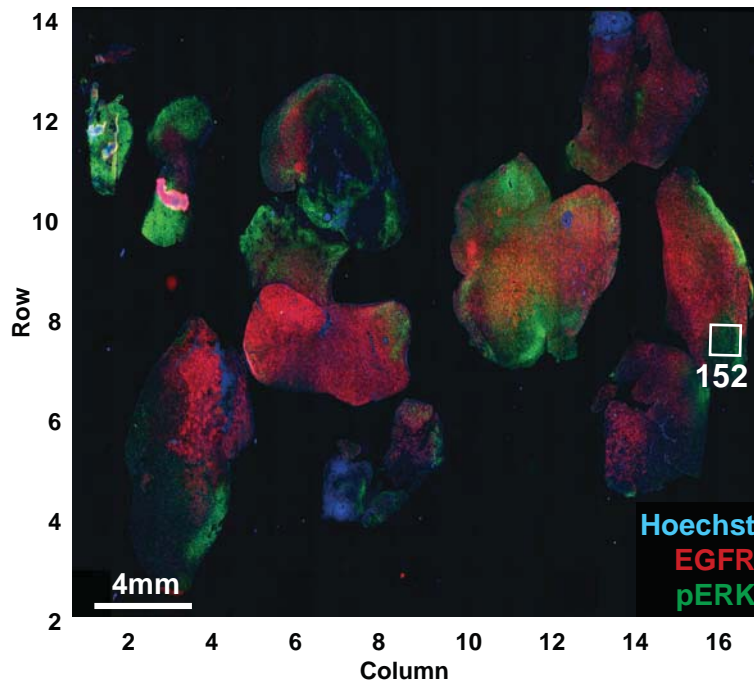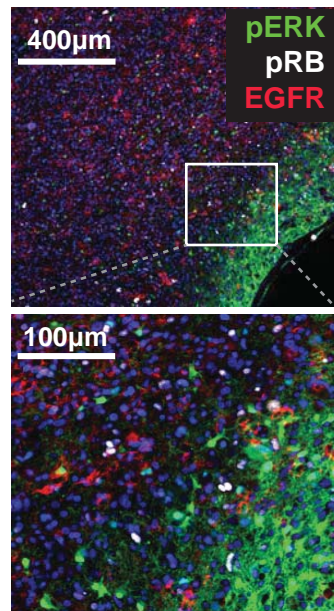
Table 1. List of antibodies tested and validated for t-CyCIF.

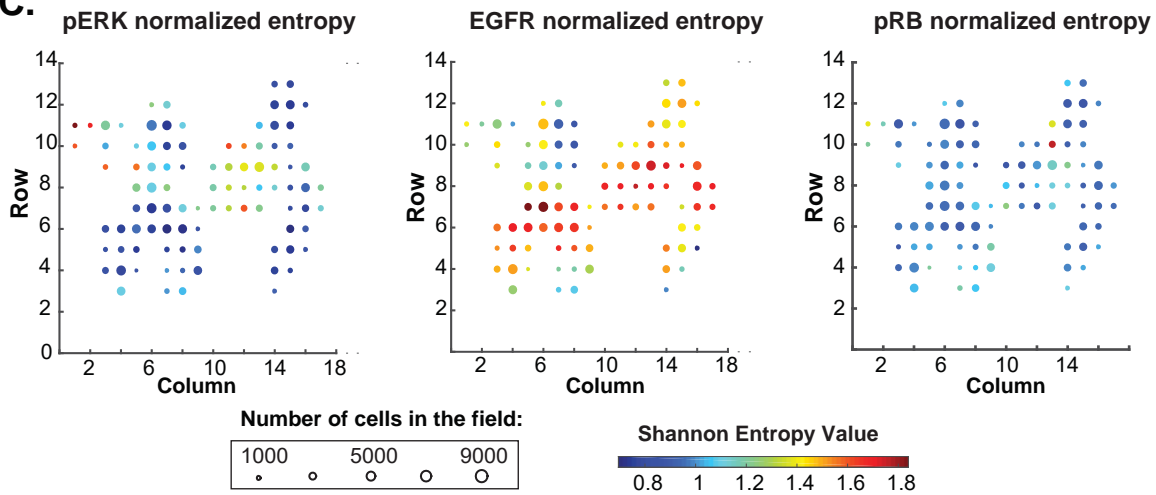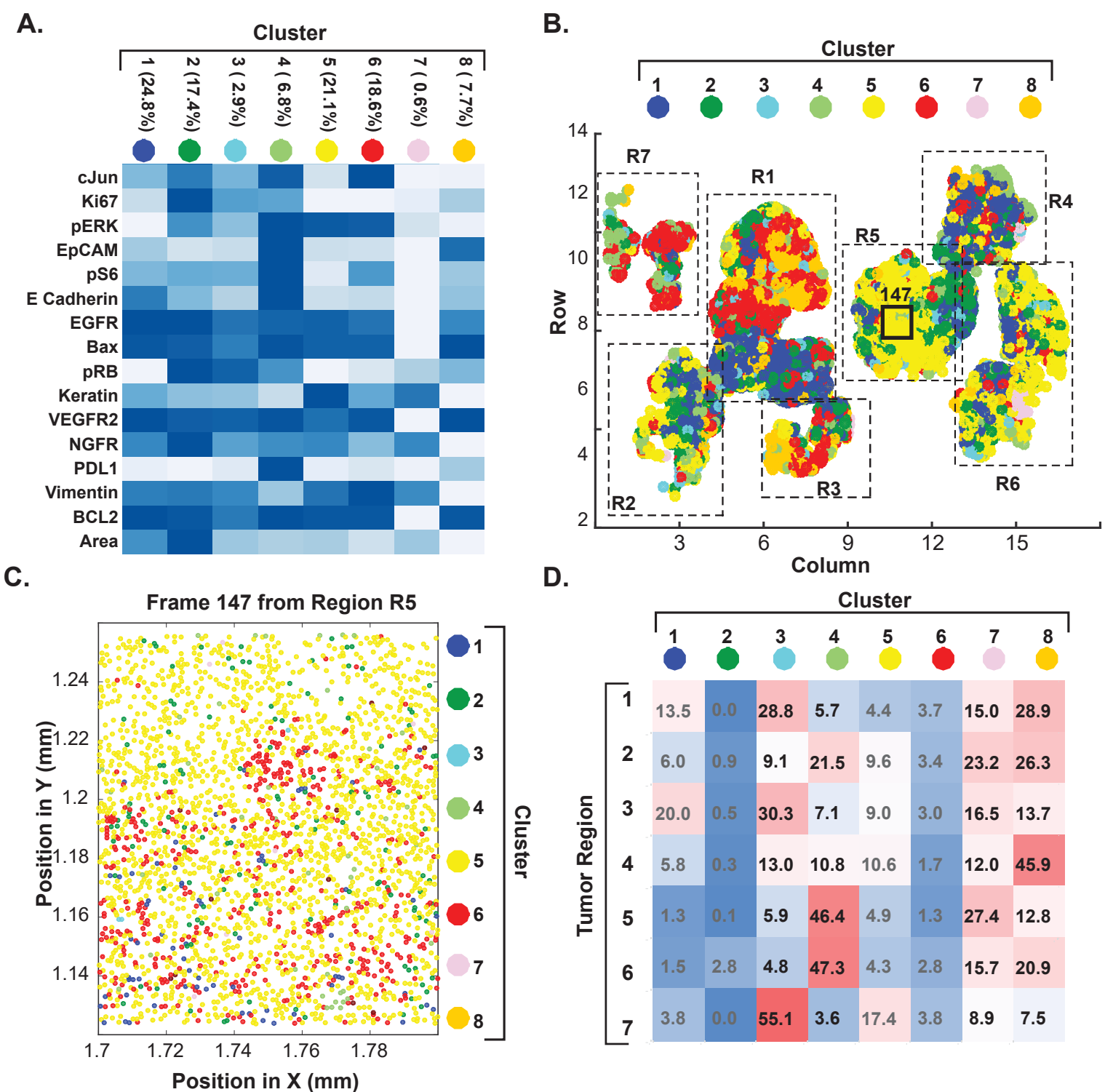| Antibody Name	Target Protein	Validation*	Vendor	Catalog no	Clone	Fluorophore	FILTER SET	Note
Bax-488	Bax	Level 2	BioLegend	633603	2D2	Alexa Fluor 488	488/FITC	
cCasp3-488	cCasp3	Level 2	R&D Systems	IC835G-025	269518	Alexa Fluor 488	488/FITC	
CD11b-488	CD11b	Level 2	Abcam	ab204271	EPR1344	Alexa Fluor 488	488/FITC	
CD4-488	CD4	Level 2	R&D Systems	FAB8165G	P01730	Alexa Fluor 488	488/FITC	
CD8a-488	CD8	Level 2	eBioscience	53-0008-80	AMC908	Alexa Fluor 488	488/FITC	
cJUN-488	cJUN	Level 2	Abcam	AB193780	E254	Alexa Fluor 488	488/FITC	
CycD1-488	CycD1	Level 2	Abcam	AB190194	EPR2241	Alexa Fluor 488	488/FITC	
Ecad-488	Ecad	Level 2	CST	3199	24E10	Alexa Fluor 488	488/FITC	
EGFR-488	EGFR	Level 2	CST	5616	D38B1	Alexa Fluor 488	488/FITC	
EpCAM-488	EpCAM	Level 2	CST	5198	VU1D9	Alexa Fluor 488	488/FITC	
HES1-488	HES1	Level 2	Abcam	AB196328	EPR4226	Alexa Fluor 488	488/FITC	
Ki67-488	Ki67	Level 2	CST	11882	D3B5	Alexa Fluor 488	488/FITC	
Lamin-488	Lamin	Level 2	CST	8617	4C11	Alexa Fluor 488	488/FITC	
MET-488	MET	Level 2	CST	8494	D1C2	Alexa Fluor 488	488/FITC	
MITF-488	MITF	Level 2	Abcam	AB201675	D5	Alexa Fluor 488	488/FITC	
mCD3E-FITC	ms_CD3E	Level 2	BioLegend	100306	145-2C11	FITC	488/FITC	
mCD4-488	ms_CD4	Level 2	BioLegend	100532	GK1.5	Alexa Fluor 488	488/FITC	
mF4/80-488	ms_F4/80	Level 2	BioLegend	123120	BM8	Alexa Fluor 488	488/FITC	
Ncad-488	Ncad	Level 2	BioLegend	350809	8C11	Alexa Fluor 488	488/FITC	
p53-488	p53	Level 2	CST	5429	7F5	Alexa Fluor 488	488/FITC	
PCNA-488	PCNA	Level 2	CST	8580	PC10	Alexa Fluor 488	488/FITC	
PD1-488	PD1	Level 2	CST	15131		Alexa Fluor 488	488/FITC	Discontinued
PDI-488	PDI	Level 2	CST	5051	C81H6	Alexa Fluor 488	488/FITC	
pERK-488	pERK	Level 2	CST	4344	D13.14.4E	Alexa Fluor 488	488/FITC	Discontinued
pNDG1-488	pNDG1	Level 2	CST	6992	D98G11	Alexa Fluor 488	488/FITC	
POL2A-488	POL2A	Level 2	Novus Biologica	NB200-598AF488	4H8	Alexa Fluor 488	488/FITC	
pS6_240-488	pS6(240/244)	Level 2	CST	5018	D68F8	Alexa Fluor 488	488/FITC	
pSQSTM-488	pSQSTM	Level 2	CST	8833	D1D9E3	Alexa Fluor 488	488/FITC	
S100a-488	S100a	Level 2	Abcam	ab207367	EPR5251	Alexa Fluor 488	488/FITC	
STAT3-488	STAT3	Level 2	CST	14047		Alexa Fluor 488	488/FITC	
Survivin-488	Survivin	Level 2	CST	2810	71G4B7	Alexa Fluor 488	488/FITC	
Actin-555	Actin	Level 2	CST	8046	13E5	Alexa Fluor 555	555/Cy3	
CD11c-570	CD11c	Level 2	eBioscience	41-9761-80	118/A5	eFluor 570	555/Cy3	
CD3-555	CD3	Level 2	Abcam	ab208514	EP4426	Alexa 555	555/Cy3	
CD4-e570	CD4	Level 2	eBioscience	41-2444-80	N1UG0	eFluor 570	555/Cy3	
CD45-PE	CD45	Level 2	R&D Systems	FAB1430P-100	2D1	PE	555/Cy3	
CD45R-e570	CD45R	Level 2	eBioscience	41-0452-80	RA3-6B2	eFluor 570	555/Cy3	
pChk2 (T68)	CHK2(pChk2)	Level 2	CST	12812	C13C1	PE	555/Cy3	
cMYC-555	cMYC	Level 2	Abcam	AB201780	Y69	Alexa Fluor 555	555/Cy3	
E2F1-555	E2F1	Level 2	Abcam	AB208078	EPR3818(3)	Alexa Fluor 555	555/Cy3	
Ecad-555	Ecad	Level 2	CST	4259		Alexa Fluor 555	555/Cy3	Discontinued
EpCAM-PE	EpCAM	Level 2	BioLegend	324205	9C4	PE	555/Cy3	
FOXO1a-555	FOXO1a	Level 2	Abcam	AB207244	EP927Y	Alexa Fluor 555	555/Cy3	
Foxp3-570	FOXP3	Level 2	eBioscience	41-4777-80	236A/E7	eFluor 570	555/Cy3	
GFAP-e570	GFAP	Level 2	eBioscience	41-9892-80	GA5	eFluor 570	555/Cy3	
HSP90-PE	HSP90b	Level 2	Abcam	AB115641	PcAb	PE	555/Cy3	
KAP1-594	KAP1	Level 2	BioLegend	619304	20A1	Alexa Fluor 594	555/Cy3	
Keratin-555	Keratin	Level 2	CST	3478	C11	Alexa Fluor 555	555/Cy3	
Keratin-570	Keratin	Level 2	eBioscience	41-9003-80	AE1/AE3	eFluor 570	555/Cy3	
Ki67-570	Ki67	Level 2	eBioscience	41-5699-80	20Raj1	eFluor 570	555/Cy3	
MAP-570	MAP2	Level 2	eBioscience	41-9763-80	AP20	eFluor 570	555/Cy3	
NFATc1-PE	NFATc1	Level 2	BioLegend	649605	7A6	PE	555/Cy3	
pAUR-555	pAUR	Level 2	CST	13464	D13A11	Alexa Fluor 555	555/Cy3	
PDL1-555	PDL1	Level 2	Abcam	AB213358	28-8	Alexa Fluor 555	555/Cy3	
pMAPK (T202/Y204)	pERK1/2(T202/Y204)	Level 2	CST	14095	197G2	PE	555/Cy3	
pH3-555	pH3	Level 2	CST	3475	D2C8	Alexa Fluor 555	555/Cy3	
pRB-555	pRB	Level 2	CST	8957	D20B12	Alexa Fluor 555	555/Cy3	
pS6(235/236)-555	pS6(235/236)	Level 2	CST	3985	D57.2.2E	Alexa Fluor 555	555/Cy3	Discontinued
pSRC-PE	pSRC	Level 2	eBioscience	12-9034-41	SC1T2M3	PE	555/Cy3	
S6-555	S6	Level 2	CST	6989	54D2	Alexa Fluor 555	555/Cy3	
VEGFR2-555	VEGFR2	Level 2	CST	12872	D5B1	Alexa Fluor 555	555/Cy3	
Vimentin-555	Vimentin	Level 2	CST	9855	D21H3	Alexa Fluor 555	555/Cy3	
Vinculin-570	Vinculin	Level 2	eBioscience	41-9777-80	7F9	eFluor 570	555/Cy3	
AKT-647	AKT	Level 2	CST	5186	C67E7	Alexa Fluor 647	647/Cy5	
aSMA-660	aSMA	Level 2	eBioscience	50-9760-80	1A4	eFluor 660	647/Cy5	
B220-Alexa647	B220	Level 2	BioLegend	103226	RA3-6B2	Alexa Fluor 647	647/Cy5	

Antibody Name	Target Protein	Validation*	Vendor	Catalog no	Clone	Fluorophore	FILTER SET Note
Bcl2-647	Bcl2	Level 2	BioLegend	658705	100	Alexa Fluor 647	647/Cy5
Catenin-647	Catenin	Level 2	CST	4627	L54E2	Alexa Fluor 647	647/Cy5
CD20-660	CD20	Level 2	eBioscience	50-0202-80	L26	eFluor 660	647/Cy5
CD45-647	CD45	Level 2	BioLegend	304020		Alexa Fluor 647	647/Cy5
CD8a-660	CD8	Level 2	eBioscience	50-0008-80	AMC908	eFluor 660	647/Cy5
ColIV-647	ColIV	Level 2	eBioscience	51-9871-80	1042	Alexa Fluor 647	647/Cy5
COXIV-647	COXIV	Level 2	CST	7561	3E11	Alexa Fluor 647	647/Cy5
FOXA2-660	FOXA2	Level 2	eBioscience	50-4778-80	3C10	eFluor 660	647/Cy5
FOXP3-647	FOXP3	Level 2	BioLegend	320113	206D	Alexa Fluor 647	647/Cy5
gH2ax-647	gH2ax	Level 2	CST	9720	20E3	Alexa Fluor 647	647/Cy5
gH2ax-647	gH2ax	Level 2	BioLegend	613407	2F3	Alexa Fluor 647	647/Cy5
hCD45	hCD45	Level 2	BioLegend	304056	H130	Alexa Fluor 647	647/Cy5
Ki67-647	Ki67	Level 2	CST	12075	D3B5	Alexa Fluor 647	647/Cy5
Ki67-647	Ki67	Level 2	BioLegend	350509	Ki-67	Alexa Fluor 647	647/Cy5
MHCI-647	MHCI	Level 2	Abcam	ab199837	EP1395Y	Alexa Fluor 647	647/Cy5
MHCII-647	MHCII	Level 2	Abcam	ab201347	EPR11226	Alexa Fluor 647	647/Cy5
mCD4-647	ms_CD4	Level 2	BioLegend	100426	GK1.5	Alexa Fluor 647	647/Cy5
mCD45-647	ms_CD45	Level 2	BioLegend	103124	30-F11	Alexa Fluor 647	647/Cy5
mEPCAM-647	ms_EPCAM	Level 2	BioLegend	118211	G8.8	Alexa Fluor 647	647/Cy5
mLy6C-647	ms_Ly6C	Level 2	BioLegend	128009	HK1.4	Alexa Fluor 647	647/Cy5
mTOR-647	mTOR	Level 2	CST	5048	7C10	Alexa Fluor 647	647/Cy5
NFkB-647	NFkB	Level 2	Abcam	AB190589	E379	Alexa Fluor 647	647/Cy5
NGFR-647	NGFR	Level 2	Abcam	AB195180	EP1039Y	Alexa Fluor 647	647/Cy5
NUP98-647	NUP98	Level 2	CST	13393	C39A3	Alexa Fluor 647	647/Cy5
p21-647	p21	Level 2	CST	8587	12D1	Alexa Fluor 647	647/Cy5
p27-647	p27	Level 2	Abcam	AB194234	Y236	Alexa Fluor 647	647/Cy5
pATM-660	pATM	Level 2	eBioscience	50-9046-41	10H11.E12	eFluor 660	647/Cy5
PDL1-647	PDL1	Level 2	CST	15005	E1L3N	Alexa Fluor 647	647/Cy5
pMK2-647	pMK2	Level 2	CST	4320	27B7	Alexa Fluor 647	647/Cy5
pmTOR-660	pmTOR	Level 2	eBioscience	50-9718-41	MRRBY	eFluor 660	647/Cy5
pS6_235-647	pS6(235/236)	Level 2	CST	4851	D57.2.2E	Alexa Fluor 647	647/Cy5
pSTAT3-647	pSTAT3	Level 2	CST	4324	D3A7	Alexa Fluor 647	647/Cy5
pTyr-647	pTyr	Level 2	CST	9415	NA	Alexa Fluor 647	647/Cy5
S100A4-647	S100A4	Level 2	Abcam	AB196168	EPR2761(2)	Alexa Fluor 647	647/Cy5
Survivin-647	Survivin	Level 2	CST	2866	71G4B7	Alexa Fluor 647	647/Cy5
TUBB3-647	TUBB3	Level 2	BioLegend	657405	AA10	Alexa Fluor 647	647/Cy5
Tubulin-647	Tubulin	Level 2	CST	3624	9F3	Alexa Fluor 647	647/Cy5
Vimentin-647	Vimentin	Level 2	BioLegend	677807	O91D3	Alexa Fluor 647	647/Cy5
anti-14-3-3	14_3_3	Level 2	Santa Cruz	SC-629-G	K-19	N/D	N/D
anti-CD11b	CD11b	Level 2	Abcam	ab133357	EPR1344	N/D	N/D
anti-CD2	CD2	Level 2	Abcam	ab37212	PcAb	N/D	N/D
anti-CD20	CD20	Level 2	Dako	M0755	L26	N/D	N/D
anti-CD3	CD3	Level 2	Dako	A0452	PcAb	N/D	N/D
anti-CD4	CD4	Level 2	Dako	M7310	M7310	N/D	N/D
anti-CD45RO	CD45RO	Level 2	Dako	M0742	UCHL1	N/D	N/D
anti-CD8	CD8	Level 2	Dako	M7103	M7103	N/D	N/D
anti-Cyclin A2	Cyclin A2	Level 2	Abcam	AB38	E23.1	N/D	N/D
anti-EDN1	EDN1	Level 2	Abcam	AB2786		N/D	N/D
anti-FAP	FAP	Level 2	eBioscience	BMS168	F11-24	N/D	N/D
anti-Flt-1	Flt	Level 2	Santa Cruz	SC-31173	N-16	N/D	N/D
anti-FOXP3	FOXP3	Level 2	BioLegend	320102	206D	N/D	N/D
anti-LAMP2	LAMP2	Level 2	Abcam	ab25631	H4B4	N/D	N/D
anti-MCM6	MCM6	Level 2	Santa Cruz	SC-9843	C-20	N/D	N/D
anti-Pax8	Pax8	Level 2	Abcam	AB191870	EPR18715	N/D	N/D
anti-PD1	PD1	Level 2	CST	86163	D4W2J	N/D	N/D
anti-pEGFR	pEGFR	Level 2	CST	3777	D7A5	N/D	N/D
anti-pRb (S807/811)	pRb(S807/811)	Level 2	Santa Cruz	SC-16670	NA	N/D	N/D
anti-pSTAT3	pSTAT3	Level 2	CST	9145		N/D	N/D
anti-TPCN2	TPCN2	Level 2	NOVUSBIO	NBP1-86923	PcAb	N/D	N/D
BrdU-488	BrdU	Level 1	BioLegend	364105	3D4	Alexa Fluor 488	488/FITC
CD11b-488	CD11b	Level 1	BioLegend	101219	M1/70	Alexa Fluor 488	488/FITC
CD123-488	CD123	Level 1	BioLegend	306035	6H6	Alexa Fluor 488	488/FITC
CD49b-FITC	CD49b	Level 1	BioLegend	359305	P1E6-C5	FITC	488/FITC
CD69	CD69	Level 1	BioLegend	310904	FN50	FITC	488/FITC
CD71-FITC	CD71	Level 1	BioLegend	334103	CY1G4	FITC	488/FITC
CD80	CD80	Level 1	R&D Systems	FAB140F	37711	FITC	488/FITC
CD80-FITC	CD80	Level 1	R&D Systems	FAB140F-025		FITC	488/FITC
cdc2-FITC	CDC2	Level 1	Santa Cruz Biot	SC-54 FITC	NA	FITC	488/FITC

Antibody Name	Target Protein	Validation*	Vendor	Catalog no	Clone	Fluorophore	FILTER SET	Note
CycB1-FITC	CycB1	Level 1	Santa Cruz Biote	SC-752 FITC	H-433	FITC	488/FITC	
FN-488	FN	Level 1	Abcam	ab198933	F1	Alexa Fluor 488	488/FITC	
IFNG-488	IFNG	Level 1	BioLegend	502517	4S.B3	Alexa Fluor 488	488/FITC	
IL1-FITC	IL1	Level 1	BioLegend	511705	H1b-98	FITC	488/FITC	
IL6-FITC	IL6	Level 1	BioLegend	501103	MQ2-13A5	FITC	488/FITC	
mCD31-FITC	ms_CD31	Level 1	eBioscience	11-0311-82	390	FITC	488/FITC	
mCD8a-488	ms_CD8a	Level 1	BioLegend	100726	53-6.7	Alexa Fluor 488	488/FITC	
Nestin-488	Nestin	Level 1	eBioscience	53-9843-80	10C2	Alexa Fluor 488	488/FITC	
p34-FITC	p34	Level 1	Santa Cruz	SC-54 FITC	17	FITC	488/FITC	
PGR-488	PGR	Level 1	Abcam	ab199224	YR85	Alexa Fluor 488	488/FITC	
Snail1-488	Snail1	Level 1	eBioscience	53-9859-80	20C8	Alexa Fluor 488	488/FITC	
TGFB-FITC	TGFB	Level 1	BioLegend	349605	TW4-2F8	FITC	488/FITC	
TNFa-488	TNFa	Level 1	BioLegend	502917	MAb11	Alexa Fluor 488	488/FITC	
AR-555	AR	Level 1	CST	8956	D6F11	Alexa Fluor 555	555/Cy3	
CD11a-PE	CD11a	Level 1	BioLegend	301207	HI111	PE	555/Cy3	
CD131-PE	CD131	Level 1	BD	559920	JORO50	PE	555/Cy3	
CD14-PE	CD14	Level 1	eBioscience	12-0149	61D3	PE	555/Cy3	
CD1a-PE	CD1a	Level 1	BioLegend	300105	HI149	PE	555/Cy3	
CD1c-PE	CD1c	Level 1	BioLegend	331505	L161	PE	555/Cy3	
CD20-PE	CD20	Level 1	BioLegend	302305	2H7	PE	555/Cy3	
CD23-PE	CD23	Level 1	eBioscience	12-0232	B3B4	PE	555/Cy3	
CD31-PE	CD31	Level 1	eBioscience	12-0319-41	WM-59	PE	555/Cy3	
CD31-PE	CD31	Level 1	R&D Systems	FAB3567P-025	9G11	PE	555/Cy3	
CD34-PE	CD34	Level 1	Abcam	ab30377	QBEND/10	PE	555/Cy3	
CD71-PE	CD71	Level 1	eBioscience	12-0711	R17217	PE	555/Cy3	
CD86-PE	CD86	Level 1	BioLegend	305405	IT2.2	PE	555/Cy3	
HER2-570	HER2	Level 1	eBioscience	41-9757-80	MJD2	eFluor 570	555/Cy3	
IL3-PE	IL3	Level 1	BD	554383	Mp2-8F8	PE	555/Cy3	
LC3-555	LC3	Level 1	CST	13173	D3U4C	Alexa Fluor 555	555/Cy3	
hPDL1-PE	PDL1	Level 1	BioLegend	329705	29E.2A3	PE	555/Cy3	
pMAPK (Y204/Y187)	pERK1/2(Y204/Y187)	Level 1	CST	75165	D1H6G	PE	555/Cy3	
pSTAT1-PE	pSTAT1	Level 1	BioLegend	686403	A15158B	PE	555/Cy3	
ABCC1-647	ABCC1	Level 1	BioLegend	370203	QCRL-2	Alexa Fluor 647	647/Cy5	
Annexin V-674	Annexin_V	Level 1	BioLegend	640911	NA	Alexa Fluor 647	647/Cy5	
CD103-647	CD103	Level 1	BioLegend	350209	Ber-ACT8	Alexa Fluor 647	647/Cy5	
CD25-647	CD25	Level 1	BioLegend	302617	BC96	Alexa Fluor 647	647/Cy5	
CD31-APC	CD31	Level 1	eBioscience	17-0319-41	WM-59	APC	647/Cy5	
CD68-APC	CD68	Level 1	BioLegend	333809	Y1/82A	APC	647/Cy5	
CD8-647	CD8	Level 1	BioLegend	344725	SK1	Alexa Fluor 647	647/Cy5	
CD8a-647	CD8	Level 1	R&D Systems	FAB1509R-025	37006	Alexa Fluor 647	647/Cy5	
CycE-660	CycE	Level 1	eBioscience	50-9714-80	HE12	eFluor 660	647/Cy5	
HIF1-647	HIF1	Level 1	BioLegend	359705	546-16	Alexa Fluor 647	647/Cy5	
HP1-647	HP1	Level 1	Abcam	AB198391	EPR5777	Alexa Fluor 647	647/Cy5	
mCD123-APC	ms_CD123	Level 1	eBioscience	17-1231-81	5B11	APC	647/Cy5	
pBTK-660	pBTK	Level 1	eBioscience	50-9015-80	M4G3LN	eFluor 660	647/Cy5	
PR-660	PR	Level 1	eBioscience	50-9764-80	KMC912	eFluor 660	647/Cy5	
PR-647	PR	Level 1	Abcam	AB199224		Alexa Fluor 647	647/Cy5	
RUNX3-660	RUNX3	Level 1	eBioscience	50-9817-80	R3-5G4	eFluor 660	647/Cy5	
SOX2-647	SOX2	Level 1	Abcam	ab192075	PcAb	Alexa Fluor 647	647/Cy5	
anti-CD11b	CD11b	Level 1	Abcam	ab52478	EP1345Y	N/D	N/D	
anti-CD8a	CD8	Level 1	eBioscience	14-0085	C8/144B	N/D	N/D	
anti-cMYC	cMYC	Level 1	BioLegend	626801	9E10	N/D	N/D	
anti-CPS1	CPS1	Level 1	Abcam	ab129076	EPR7493-3	N/D	N/D	
anti-E2F1	E2F1	Level 1	Thermo	MS-879-P1	KH95	N/D	N/D	
anti-eEF2K	eEF2K	Level 1	Santa Cruz	SC-21642	K-19	N/D	N/D	
anti-Emil1	Emil1	Level 1	Abcam	ab18341	PcAb	N/D	N/D	
anti-ET1	ET1	Level 1	Abcam	ab2786	TR.ET.48.5	N/D	N/D	
anti-FKHRL1	FKHRL1	Level 1	Santa Cruz	SC-9812	S-20	N/D	N/D	
anti-FLAG	FLAG	Level 1	Sigma	F1804	M2	N/D	N/D	
anti-GranB	Granzyme_B	Level 1	Dako	M7235	M7235	N/D	N/D	
anti-HMB45	HMB45	Level 1	Abcam	ab732	01+BC199	N/D	N/D	
anti-HSP90b	HSP90b	Level 1	Santa Cruz	SC-1057	D-19	N/D	N/D	
anti-IL2Ra	IL2Ra	Level 1	Abcam	ab128955	EPR6452	N/D	N/D	
anti-LC3B	LC3	Level 1	Abcam	AB81785	PcAb	N/D	N/D	
anti-MiTF	MiTF	Level 1	Abcam	ab80651	C5	N/D	N/D	
anti-Ncad	Ncad	Level 1	Abcam	AB18203	PcAb	N/D	N/D	
anti-NCAM	NCAM	Level 1	Abcam	ab6123	ERIC-1	N/D	N/D	
anti-NF1	NF1	Level 1	Abcam	AB178323	McNFn27b	N/D	N/D	

Antibody Name	Target Protein	Validation*	Vendor	Catalog no	Clone	Fluorophore	FILTER SET	Note
anti-PD1	PD1	Level 1	CST	43248	EH33	N/D	N/D	
anti-pHsp90b	pHsp90b	Level 1	Abcam	ab63562	PcAb	N/D	N/D	
anti-pTuberin	pTuberin	Level 1	Abcam	ab133465	EPR8202	N/D	N/D	
anti-RFP	RFP	Level 1	Thermo	R10367	PcAb	N/D	N/D	
anti-SirT3	SirT3	Level 1	CST	2627	C73E3	N/D	N/D	
anti-TIA1	TIA1	Level 1	Santa Cruz	SC-1751	PcAb	N/D	N/D	
anti-TLR3	TLR3	Level 1	Santa Cruz	SC-8692		N/D	N/D	
anti-TNFa	TNFa	Level 1	Abcam	AB11564	MP6-XT3	N/D	N/D	
CD11a-FITC	CD11a	Level 0	eBioscience	11-0119-41	HI111	FITC	488/FITC	
CD2-FITC	CD2	Level 0	BioLegend	300206	RPA-2.10	FITC	488/FITC	
CD20-FITC	CD20	Level 0	BioLegend	302303	2H7	FITC	488/FITC	
CD8a-488	CD8	Level 0	BioLegend	301024	RPA-T8	Alexa Fluor 488	488/FITC	
c-Jun-FITC	cJUN	Level 0	Santa Cruz Biotec	SC-1694 FITC	H-79	FITC	488/FITC	
Ecad-FITC	Ecad	Level 0	BioLegend	324103	67A4	FITC	488/FITC	
FOXP3-488	FOXP3	Level 0	BioLegend	320011	150D	Alexa Fluor 488	488/FITC	
MITF-488	MITF	Level 0	Novus Biologica	NB100-56561AF488	21D1418	Alexa Fluor 488	488/FITC	
NGFR-FITC	NGFR	Level 0	BioLegend	345103	ME20.4	FITC	488/FITC	
PD1-488	PD1	Level 0	BioLegend	329935	EH12.2H7	Alexa Fluor 488	488/FITC	
hPD-1-488	PD1	Level 0	BioLegend	367407	NAT105	Alexa Fluor 488	488/FITC	
pERK(m)-488	pERK(m)	Level 0	CST	4374	E10	Alexa Fluor 488	488/FITC	
S100A4-FITC	S100A4	Level 0	BioLegend	370007	NJ-4F3-D1	FITC	488/FITC	
SOX2-488	SOX2	Level 0	BioLegend	656109	14A6A34	Alexa Fluor 488	488/FITC	
CD133-PE	CD133	Level 0	eBioscience	12-1338-41	TMP4	PE	555/Cy3	
cMyc-TRITC	cMYC	Level 0	Santa Cruz Biotec	SC-40 TRITC	9E10	TRITC	555/Cy3	
cPARP-555	cPARP	Level 0	CST	6894		Alexa Fluor 555	555/Cy3	Discontinued
CTLA4-PE	CTLA4	Level 0	BioLegend	369603	BNI3	PE	555/Cy3	
GATA3-594	GATA3	Level 0	BioLegend	653816	16E10A23	Alexa Fluor 594	555/Cy3	
Oct4-555	OCT_4	Level 0	CST	4439	C30A3	Alexa Fluor 555	555/Cy3	
p21-555	p21	Level 0	CST	8493		Alexa Fluor 555	555/Cy3	Discontinued
PD1-PE	PD1	Level 0	BioLegend	329905	EH12.2H7	PE	555/Cy3	
PDGFRb-555	PDGFRb	Level 0	Abcam	AB206874	Y92	Alexa Fluor 555	555/Cy3	
pSTAT1-555	pSTAT1	Level 0	CST	8183	58D6	Alexa Fluor 555	555/Cy3	
TIM1-PE	TIM1	Level 0	BioLegend	353903	1D12	PE	555/Cy3	
CD103-APC	CD103	Level 0	eBioscience	17-1038-41	B-Ly7	APC	647/Cy5	
CD3-647	CD3	Level 0	BioLegend	300422	UCHT1	Alexa Fluor 647	647/Cy5	
CD3-APC	CD3	Level 0	eBioscience	17-0038-41	UCHT1	APC	647/Cy5	
CD3-660	CD3	Level 0	eBioscience	50-0037-41	OKT3	eFluor 660	647/Cy5	
FOXO3a-647	FOXO3a	Level 0	Abcam	AB196539	EP1949Y	Alexa Fluor 647	647/Cy5	
GrB-647	Granzyme_B	Level 0	BioLegend	515405	GB11	Alexa Fluor 647	647/Cy5	
GrB-APC	Granzyme_B	Level 0	R&D Systems	IC29051A	356412	APC	647/Cy5	
HER2-647	HER2	Level 0	BioLegend	324412	24D2	Alexa Fluor 647	647/Cy5	
mCD49b-647	ms_CD49b	Level 0	BioLegend	103511	HMα2	Alexa Fluor 647	647/Cy5	
NCAM-647	NCAM	Level 0	BioLegend	362513	5.1H11	Alexa Fluor 647	647/Cy5	
pAKT-647	pAKT	Level 0	CST	4075	D9E	Alexa Fluor 647	647/Cy5	
pERK(m)-647	pERK(m)	Level 0	CST	4375	E10	Alexa Fluor 647	647/Cy5	
pERK1/2 (T202/Y204)	pERK1/2 (T202/Y204)	Level 0	BioLegend	369503	6B8B69	Alexa Fluor 647	647/Cy5	
pIKBa-660	pIKBa	Level 0	eBioscience	50-9035-41	RILYB3R	eFluor 660	647/Cy5	
anti-AXL	AXL	Level 0	CST	8661	C89E7	N/D	N/D	
CD11C-BV570	CD11C	Level 0	BioLegend	117331	N418	BV570	N/D	
CD45-785	CD45	Level 0	BioLegend	304047	HI30	BV785	N/D	
anit-pcJUN	cJUN(pcJUN)	Level 0	Santa Cruz	SC-822	KM-1	N/D	N/D	
LY6G-570	LY6G	Level 0	BioLegend	127629	1A8	BV570	N/D	
anti-TPCN2	TPCN2	Level 0	Abcam	ab119915	PcAb	N/D	N/D	

*Level 2: Show positive/correct signals in mutliple samples/tissues
*Level 1: Show positive/correct signals in few but not all samples tested
*Level 0: show no signal or incorrect signals in all samples tested
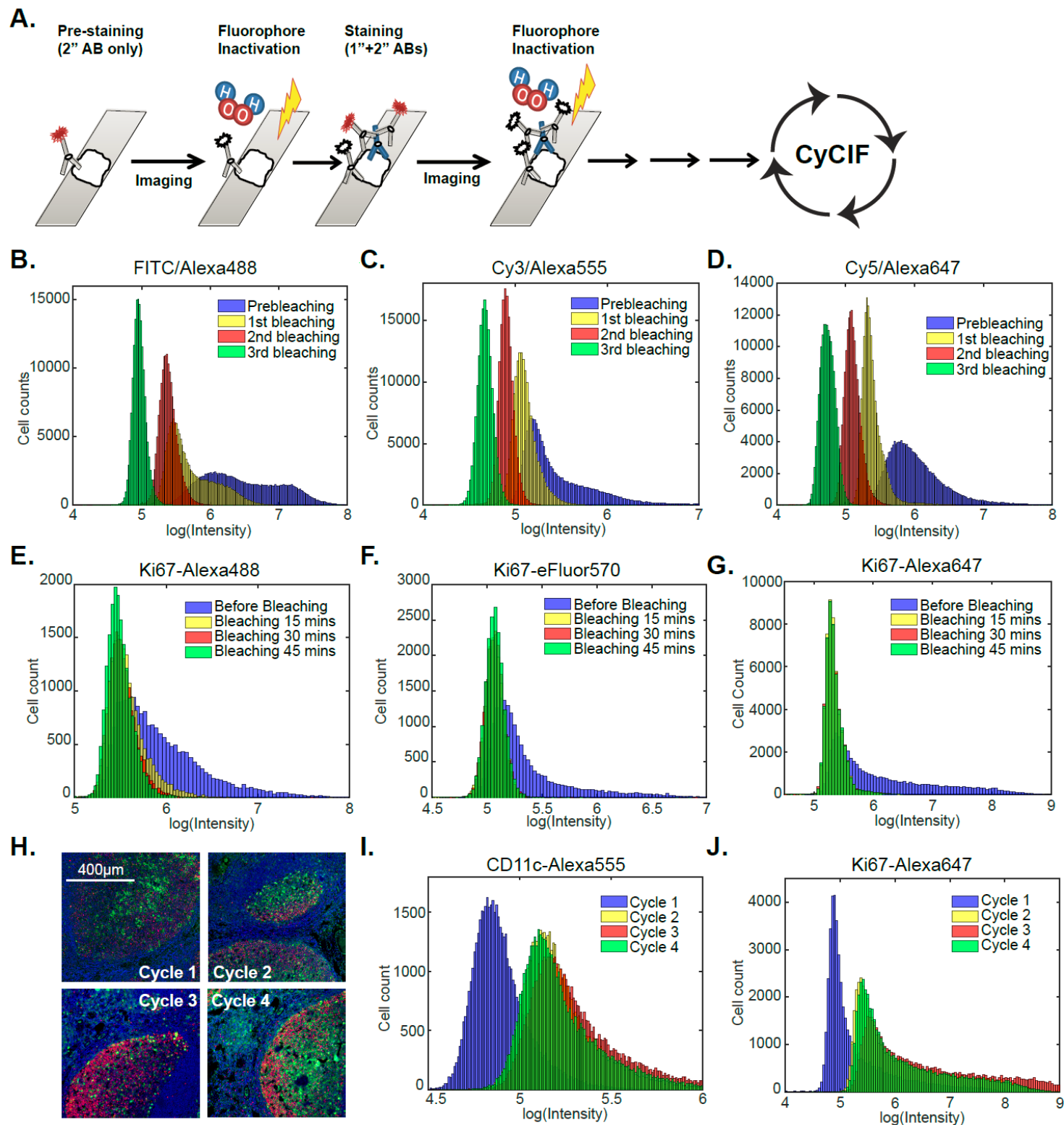
Supplementary Figure S1. Technical aspects of the t-CyCIF process (Covering data in Figures 1 and 2).

(A) Schematic of pre-processing steps for t-CyCIF. **(B-D)** Evaluation of auto-fluorescence and fluorophore

inactivation. Tonsil tissue was stained with Hoechst 33342 and imaged in all four channels before and after 3

cycles of fluorophore inactivation. **(E and F)**. Single-cell quantification of fluorophore inactivation in tonsil

tissue stained with antibodies indicated. **(H-J).** The effect of repeated rounds of fluorophore inactivation on

antigenicity. Tonsil tissue was stained with Ki67-Alexa647 (colored red in **H**) and CD11c-Alexa 555

antibodies (colored green in **H**). The intensities were measured after 1, 2, 3, and 4 cycles of fluorophore

inactivation. **(I and J)** Distributions of single-cell fluorescence intensities measured in (H) from different

cycles are shown.
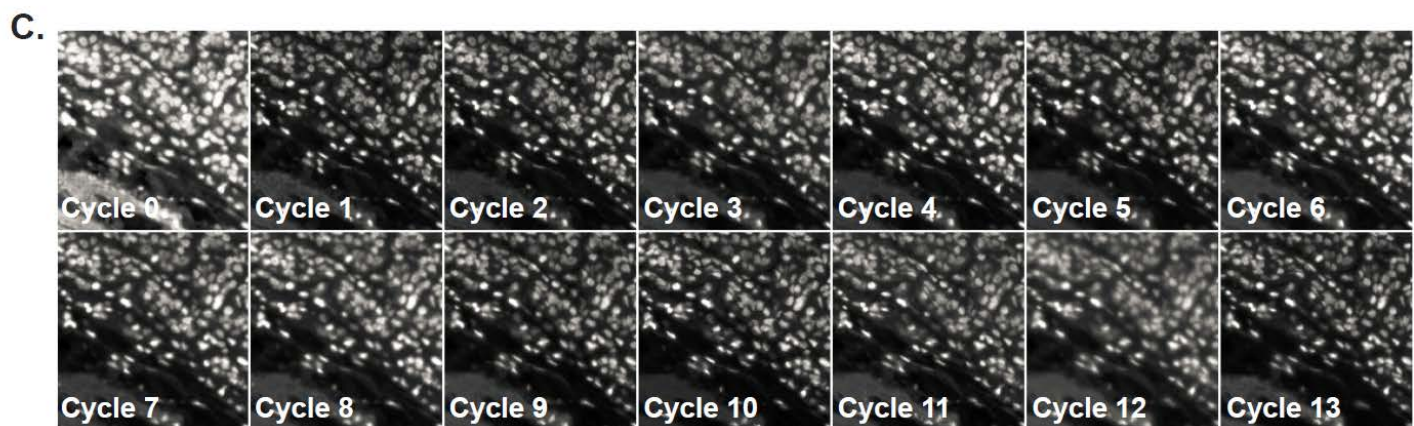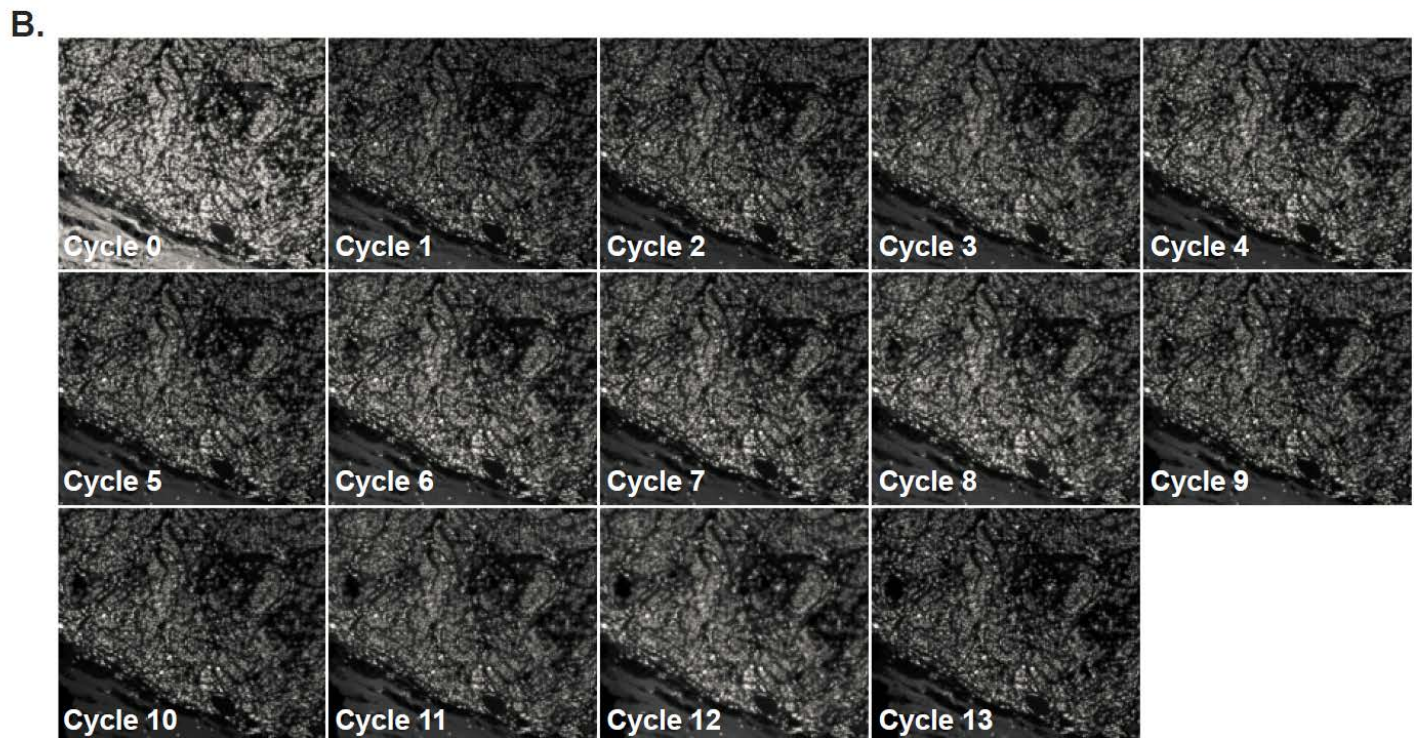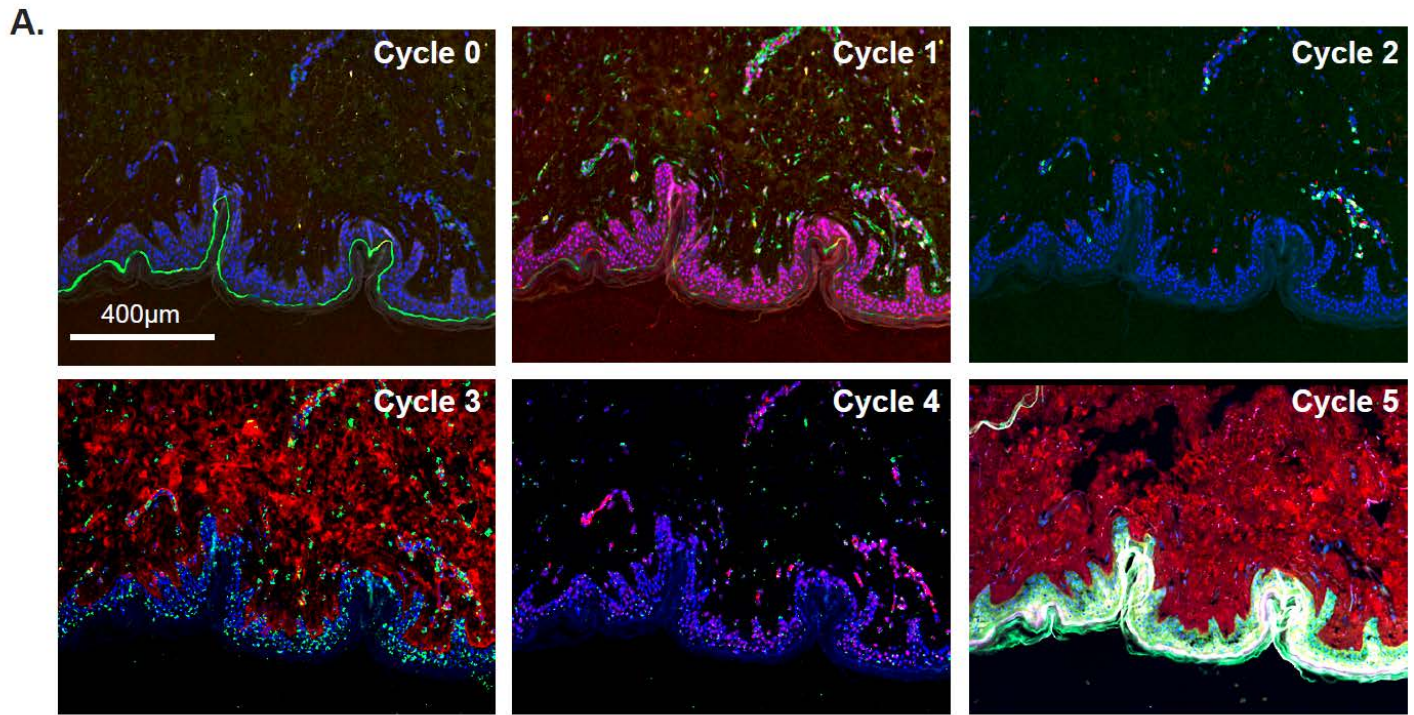
Supplementary Figure S2. Retention of tissue ultra-structure during t-CyCIF (Covering data in Figure 2).

(A) Normal skin imaged with 5-cycle t-CyCIF with as indicated. **(B)** Melanoma samples imaged via 14 cycle t-CyCIF showing the (pseudo-colored) Hoechst channel only as a means to judge tissue integrity. Cycle 0 denotes the pre-staining cycle. **(C)** Higher magnification view of the sample images of (B).
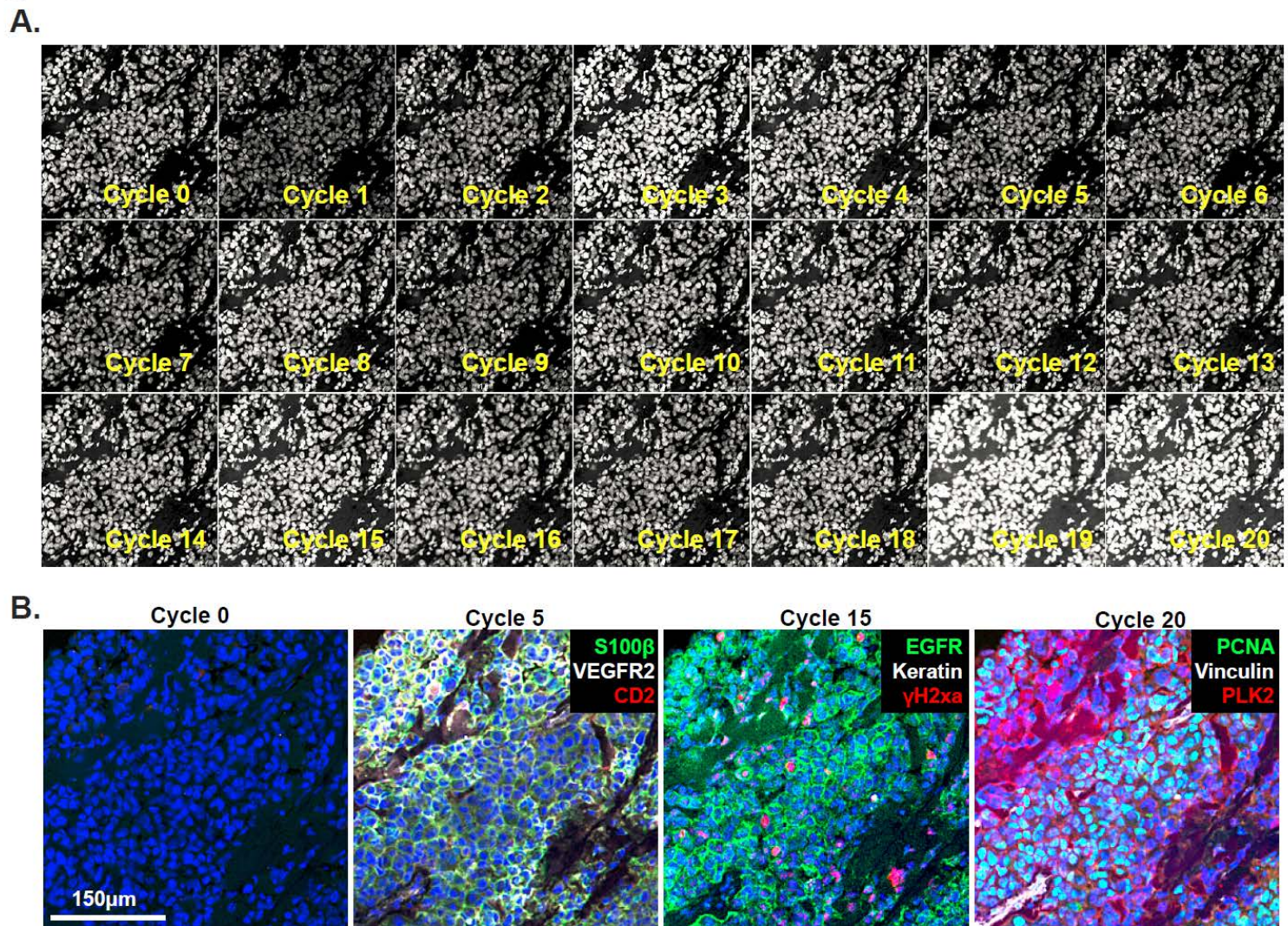
Supplementary Figure S3. 60-marker t-CyCIF in a melanoma tumor. (A) Gallery of pseudo-colored cycles of a melanoma specimen that underwent 20 cycles of t-CyCIF. **(B)** Representative cycles 0, 5, 10 and 20 of the specimen from panel (A) highlighting markers of various biological processes, such as cancer cell autonomous expression of angiogenesis receptor VEGFR2, DNA damage (i.e. γH2xa), receptor tyrosine kinase (i.e. EGFR) and cell cycle markers (i.e. PCNA).
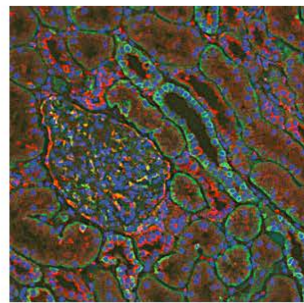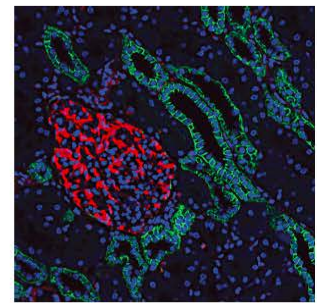
A. Normal Kidney
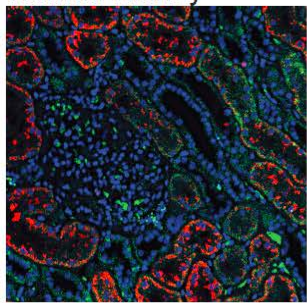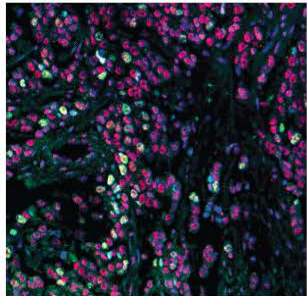

Green: Ki67
Red: p21
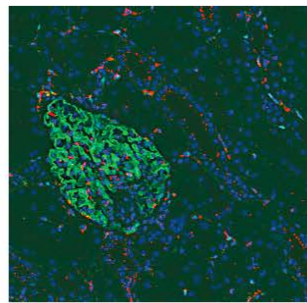
Green: p-ERK
Red: p-S6(235/236)

Green: EGFR
Red: VEGFR2

Green: E-Cadherin
Red: Vimentin

B. Breast Invasive tubular mixed carcinoma

Green: Ki67
Red: p-CTD(S2)
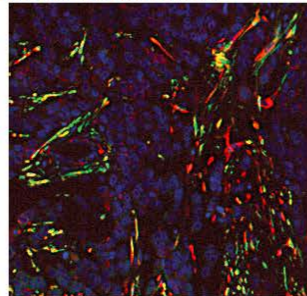
Green: p-ERK
Red: p-S6(235/236)
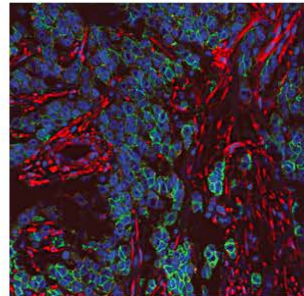
Green: EGFR
Red: VEGFR2
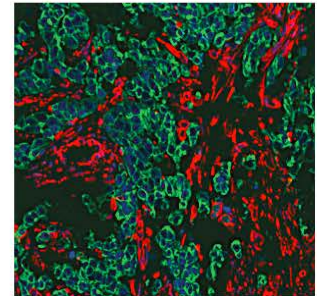
Green: Keratin
Red: Vimentin

C. Lymph node (Reactive)
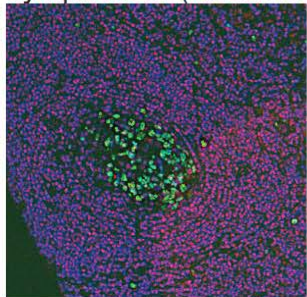
Green: Ki67
Red: p-CTD(S2)
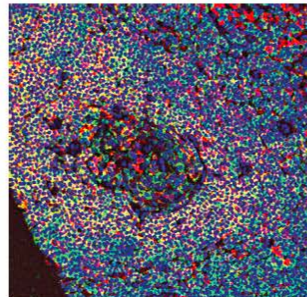
Green: CD45
Red: pS6(235/236)
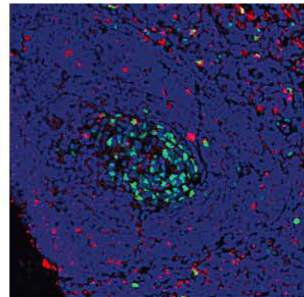
Green: PCNA
Red: PD-L1
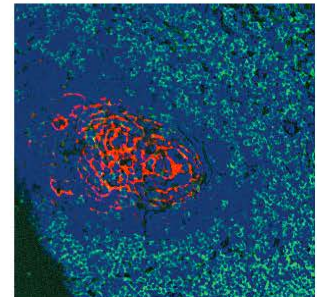
Green: CD4
Red: NGFR

D. Melanoma, grade II
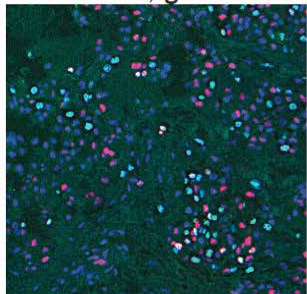
Green: Ki67
Red: p21
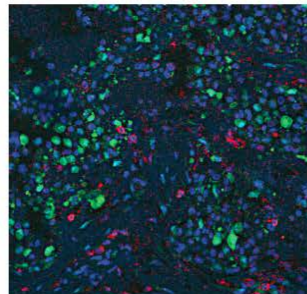
Green: p-ERK
Red: CD45
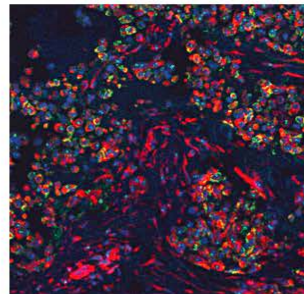
Green: E-Cadherin
Red: Vimentin
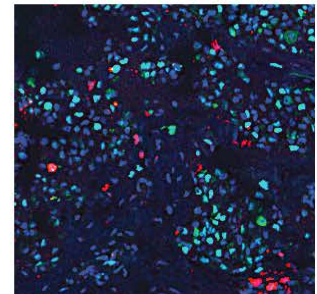
Green: PCNA
Red: PD-L1

Supplementary Figure S4. Imaging of tissue microarrays by t-CyCIF (covering data in Figure 4). Gallery of additional representative images of 8-cyle t-CyCIF of biopsies in a tissue microarray.
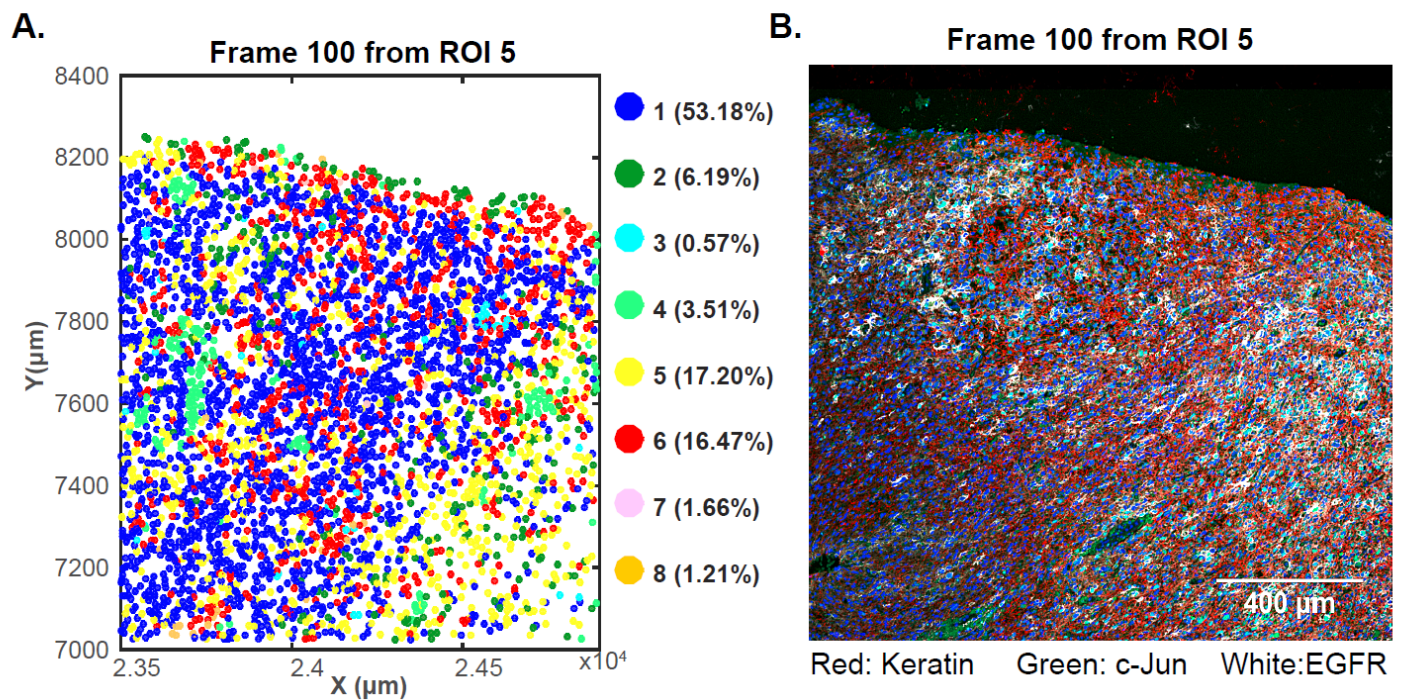
Supplementary Figure S5. Cell-to-cell heterogeneity in a GBM tumor (covering data in Figure 6) **(A)** EMGM clusters (as defined and color-coded in Figure 6) frame 100 in tumor region R5 mapped onto the positions of single cells. The percentage of cells in each cluster is shown. **(B).** Representative image of the same frame for cytokeratin, c-Jun and EGFR staining.

Table S1. List of antibodies used to stain tonsil tissue presented in Figure 2

Cycle	Ch/Filter	Antibody Name	Target	Vendor	Catalog no	Clone	Fluorophore
1	488/FITC	CD4-488	CD4	R&D	FAB8165G	P01730	Alexa Fluor 488
1	555/Cy3	Ki67-570	Ki67	eBioscience	41-5699-80	20Raj1	eFluor 570
1	647/Cy5	AKT-647	AKT	CST	5186	C67E7	Alexa Fluor 647
2	488/FITC	CD8a-488	CD8	eBioscience	53-0008-80	AMC908	Alexa Fluor 488
2	555/Cy3	CD45R-e570	CD45R	eBioscience	41-0452-80	RA3-6B2	eFluor 570
2	647/Cy5	CD3-660	CD3	eBioscience	50-0037-41	OKT3	eFluor 660
3	488/FITC	PD1-488	PD1	CST	15131	n/d	Alexa Fluor 488
3	555/Cy3	CD45-PE	CD45	R&D	FAB1430P-	2D1	PE
3	647/Cy5	PDL1-647	PDL1	CST	15005	E1L3N	Alexa Fluor 647
4	488/FITC	PCNA-488	PCNA	CST	8580	PC10	Alexa Fluor 488
4	555/Cy3	Foxp3-570	FOXP3	eBioscience	41-4777-80	236A/E7	eFluor 570
4	647/Cy5	Bcl2-647	Bcl2	BioLegend	658705	100	Alexa Fluor 647
5	488/FITC	Ecad-488	Ecad	CST	3199	24E10	Alexa Fluor 488
5	555/Cy3	NFATc1-PE	NFATc1	BioLegend	649605	7A6	PE
5	647/Cy5	Vimentin-647	Vimentin	BioLegend	677807	O91D3	Alexa Fluor 647
6	488/FITC	Lamin-488	Lamin	CST	8617	4C11	Alexa Fluor 488
6	555/Cy3	FOXO1a-555	FOXO1a	Abcam	AB207244	EP927Y	Alexa Fluor 555
6	647/Cy5	NFkB-647	NFkB	Abcam	AB190589	E379	Alexa Fluor 647
7	488/FITC	Bax-488	Bax	BioLegend	633603	2D2	Alexa Fluor 488
7	555/Cy3	Actin-555	Actin	CST	8046	13E5	Alexa Fluor 555
7	647/Cy5	Ki67-647	Ki67	BioLegend	350509	Ki-67	Alexa Fluor 647
8	488/FITC	HES1-488	HES1	Abcam	AB196328	EPR4226	Alexa Fluor 488
8	555/Cy3	cMYC-555	cMYC	Abcam	AB201780	Y69	Alexa Fluor 555
8	647/Cy5	p27-647	p27	Abcam	AB194234	Y236	Alexa Fluor 647
9	488/FITC	FN-488	FN	Abcam	ab198933	F1	Alexa Fluor 488
9	555/Cy3	Vinculin-570	Vinculin	eBioscience	41-9777-80	7F9	eFluor 570
9	647/Cy5	pTyr-647	pTyr	CST	9415	n/d	Alexa Fluor 647
10	488/FITC	STAT3-488	STAT3	CST	14047	n/d	Alexa Fluor 488
10	555/Cy3	CD34-PE	CD34	Abcam	ab30377	QBEND/10	PE
10	647/Cy5	SOX2-647	SOX2	Abcam	ab192075	PcAb	Alexa Fluor 647

Table S2. List of antibodies used to stain PDAC sample presented in Figure 3 and TMA in Figure 4.

Cycle	Ch/Filter	Antibody Name	Target Protein	Vendor	Catalog no	Clone	Fluorophore
1	488/FITC	anti-pAKT	pAKT	CST	4060	D9E	anti-Rabbit (Alexa 488)
1	555/Cy3	anti-pCTD2	pCTD2	Active Motif	61084	3E10	anti-Rat (Alexa 555)
1	647/Cy5	anti-5hmC	5hmc	Active Motif	40000	59.1	anti-Mouse (Alexa 647)
2	488/FITC	Ki67	Ki67-488	Ki67	CST	11882	Alexa Fluor 488
2	555/Cy3	Oct4-555	OCT_4	CST	4439	C30A3	Alexa Fluor 555
2	647/Cy5	p21	p21-647	p21	CST	8587	Alexa Fluor 647
3	488/FITC	pERK-488	pERK	CST	4344	D13.14.4E	Alexa Fluor 488
3	555/Cy3	CD45-PE	CD45	R&D Systems	FAB1430P-100	2D1	PE
3	647/Cy5	pS6_235-647	pS6(235/236)	CST	4851	D57.2.2E	Alexa Fluor 647
4	488/FITC	EGFR-488	EGFR	CST	5616	D38B1	Alexa Fluor 488
4	555/Cy3	VEGFR2-555	VEGFR2	CST	12872	D5B1	Alexa Fluor 555
4	647/Cy5	HER2-647	HER2	BioLegend	324412	24D2	Alexa Fluor 647
5	488/FITC	Ecad-488	Ecad	CST	3199	24E10	Alexa Fluor 488
5	555/Cy3	Keratin-555	Keratin	CST	3478	C11	Alexa Fluor 555
5	647/Cy5	Vimentin-647	Vimentin	BioLegend	677807	O91D3	Alexa Fluor 647
6	488/FITC	PCNA-488	PCNA	CST	8580	PC10	Alexa Fluor 488
6	555/Cy3	PDL1-555	PDL1	Abcam	AB213358	28-8	Alexa 555
6	647/Cy5	Catenin-647	Catenin	CST	4627	L54E2	Alexa Fluor 647
7	488/FITC	MET-488	MET	CST	8494	D1C2	Alexa Fluor 488
7	555/Cy3	CD4-e570	CD4	eBioscience	41-2444-80	N1UG0	eFluor 570
7	647/Cy5	NGFR-647	NGFR	Abcam	AB195180	EP1039Y	Alexa Fluor 647
8	488/FITC	Mitotracker	N/D	Invitrogen	M7514	N/D	N/A
8	555/Cy3	ActinRed	N/D	Invitrogen	R37112	N/D	Alexa Fluor 555
8	647/Cy5	HCSred	N/D	Invitrogen	H32714	N/D	N/A

Table S3. Description and naming convention of TMA used in Figure 4.

Abbreviation	Anatomic site	Age	Sex	Histology	Stage (TNM)	Image Name
BL1	Bladder	45	M	Normal bladder, tiny tissue fragment or tissue missing	-	Composite-TMA-0
BL2	Bladder	80	M	Transitional cell carcinoma, grade I~II	T2N0M0	Composite-TMA-1
BL3	Bladder	51	M	Transitional cell carcinoma, grade II	T1N0M0	Composite-TMA-2
BR1	Breast	38	F	Normal breast	-	Composite-TMA-3
BR2	Breast	37	F	Invasive tubular mixed carcinoma	T1N1M0	Composite-TMA-4
BR3	Breast	43	F	Invasive ductual carcinoma	T2N1M0	Composite-TMA-5
ST1	GI-Stomach	71	M	Normal stomach	-	Composite-TMA-6
ST2	GI-Stomach	69	F	Adenocarcinoma, grade I~II	T2N1M0	Composite-TMA-7
ST3	GI-Stomach	65	M	Adenocarcinoma, grade II~III	T3N1M0	Composite-TMA-8
CO1	GI-Colonrectal	10/12	F	Normal colon	-	Composite-TMA-9
CO2	GI-Colonrectal	60	F	Colon carcinoma, grade II	T2N1M1	Composite-TMA-10
CO3	GI-Colonrectal	85	F	Rectal carcinoma, grade II~III	T2N0M0	Composite-TMA-11
KI1	Kidney	2	F	Normal kidney cortex	-	Composite-TMA-12
KI2	Kidney	53	F	Clear cell carcinoma, grade II	T1N0M0	Composite-TMA-13
KI3	Kidney	44	M	Cear cell carcinoma, grade III	T1N0M0	Composite-TMA-14
LI1	Liver	52	M	Normal	-	Composite-TMA-15
LI2	Liver	33	M	Hepatocellular carcinoma, grade II~II	T2N0M0	Composite-TMA-16
LI3	Liver	47	M	Hepatocellular carcinoma, grade I~II	T2N0M0	Composite-TMA-17
LU1	Lung	60	M	Normal lung	-	Composite-TMA-18
LU2	Lung	69	M	Squamous cell carcinoma, grade II~III	T2N0M0	Composite-TMA-19
LU3	Lung	70	M	Adenocarcinoma, grade II	T2N1M0	Composite-TMA-20
LY1	Lymph node	39	F	Reactive	-	Composite-TMA-21
LY2	Lymph node	40	M	Hodgkin's lymphoma	-	Composite-TMA-22
LY3	Lymph node	77	F	NHL-B	-	Composite-TMA-23
OV1	Ovary	16	F	Normal ovary	-	Composite-TMA-24
OV2	Ovary	20	F	Adenocarcinoma, grade I~II	T2N0M0	Composite-TMA-25
OV3	Ovary	45	F	Adenocarcinoma, grade III	T2aN0M0	Composite-TMA-26
PA1	Pancreas	46	M	Normal pancreas	-	Composite-TMA-27
PA2	Pancreas	64	F	Adenocarcinoma, grade I~II	T1N0M0	Composite-TMA-28
PA3	Pancreas	49	F	Adenocarcinoma, grade II~III	T1N0M0	Composite-TMA-29
PR1	Prostate	74	M	Pro	-	Composite-TMA-30
PR2	Prostate	54	M	Transitional cell carcinoma, grade II	T1N0M0	Composite-TMA-31
PR3	Prostate	60	M	Adenocarcinoma, grade II	T1N0M0	Composite-TMA-32
SK1	Skin	48	F	Normal skin	-	Composite-TMA-33
SK2	Back skin	67	M	Squamous cell carcinoma, grade II	T2N0M0	Composite-TMA-34
SK3	Skin	49	M	Melanoma, grade II	T2N0M0	Composite-TMA-35
UT1	Uterus	47	F	Normal uterus	-	Composite-TMA-36
UT2	Uterus	43	F	Cervical squamous cell carcinoma, grade II	T1N0M0	Composite-TMA-37
UT3	Uterus	44	F	Endometrial adenocarcinoma, grade II	T1bN0M0	Composite-TMA-38

Table S4 List of antibodies used to stain RCC tissue presented in Figure 3

Cycle	Ch/Filter	Antibody Name	Target Protein	Vendor	Catalog no	Clone	Fluorophore
1	488/FITC	anti-CD3	CD3	Dako	A0452	PcAb	anti-Rabbit (Alexa 488)
1	555/Cy3	anti-Flt1	Flt	Santa Cruz	SC-31173	N-16	anti-Goat (Alexa 555)
1	647/Cy5	anti-CD8a	CD8	eBioscience	14-0085	C8/144B	anti-Mouse (Alexa 647)
2	488/FITC	MITF-488	MITF	Abcam	AB201675	D5	Alexa Fluor 488
2	555/Cy3	PDL1-555	PDL1	Abcam	AB213358	28-8	Alexa Fluor 555
2	647/Cy5	S100A4-647	S100A4	Abcam	AB196168	EPR2761(2)	Alexa Fluor 647
3	488/FITC	anti-NF1	NF1	Abcam	AB178323	McNFn27b	Zenon-488
3	555/Cy3	anti-Pax8	Pax8	Abcam	AB191870	EPR18715	Zenon-555
3	647/Cy5	anti-Ncad	Ncad	Abcam	AB18203	PcAb	Zenon-647
4	488/FITC	PD1-488	PD1	CST	15131	n/d	Alexa Fluor 488
4	555/Cy3	CD4-e570	CD4	eBioscience	41-2444-80	N1UG0	eFluor 570
4	647/Cy5	PDL1-647	PDL1	CST	15005	E1L3N	Alexa Fluor 647
5	488/FITC	pS6_240-488	pS6(240/244)	CST	5018	D68F8	Alexa Fluor 488
5	555/Cy3	CD45-PE	CD45	R&D Systems	FAB1430P-100	2D1	PE
5	647/Cy5	anti-CD3	CD3	Dako	A0452	PcAb	Zenon-647
6	488/FITC	EGFR-488	EGFR	CST	5616	D38B1	Alexa Fluor 488
6	555/Cy3	VEGFR2-555	VEGFR2	CST	12872	D5B1	Alexa Fluor 555
6	647/Cy5	anti-CD45RO	CD45RO	Dako	M0742	UCHL1	Zenon-647
7	488/FITC	MET-488	MET	CST	8494	D1C2	Alexa Fluor 488
7	555/Cy3	AR-555	AR	CST	8956	D6F11	Alexa Fluor 555
7	647/Cy5	pSTAT3-647	pSTAT3	CST	4324	D3A7	Alexa Fluor 647
8	488/FITC	Ecad-488	Ecad	CST	3199	24E10	Alexa Fluor 488
8	555/Cy3	CD86-PE	CD86	BioLegend	305405	IT2.2	PE
8	647/Cy5	Vimentin-647	Vimentin	BioLegend	677807	O91D3	Alexa Fluor 647
9	488/FITC	Nestin-488	Nestin	eBioscience	53-9843-80	10C2	Alexa Fluor 488
9	555/Cy3	CD31-PE	CD31	eBioscience	12-0319-41	WM-59	PE
9	647/Cy5	CD31-APC	CD31	eBioscience	17-0319-41	WM-59	APC
10	488/FITC	PCNA-488	PCNA	CST	8580	PC10	Alexa Fluor 488
10	555/Cy3	Keratin-570	Keratin	eBioscience	41-9003-80	AE1/AE3	eFluor 570
10	647/Cy5	TUBB3-647	TUBB3	BioLegend	657405	AA10	Alexa Fluor 647
11	488/FITC	p53-488	p53	CST	5429	7F5	Alexa Fluor 488
11	555/Cy3	anti-FAP	FAP	eBioscience	BMS168	F11-24	Zenon-555
11	647/Cy5	aSMA-660	aSMA	eBioscience	50-9760-80	1A4	eFluor 660
12	488/FITC	Mitotracker	n/d	Invitrogen	M7514	n/d	N/A
12	555/Cy3	ActinRed	n/d	Invitrogen	R37112	n/d	Alexa Fluor 555
12	647/Cy5	HCSred	n/d	Invitrogen	H32714	n/d	N/A

Table S5. List of antibodies used to stain GBM tissue presented in Figure 5 and Figure 6.

Cycle	Ch/Filter	Antibody Name	Target Protein	Vendor	Catalog no	Clone	Fluorophore
1	488/FITC	anit-pcJUN	cJUN(pcJUN)	Santa Cruz	SC-822	KM-1	anti-Rabbit (Alexa 488)
1	555/Cy3	anti-AXL	AXL	R&D	AF154	n/d	anti-Goat (Alexa 555)
1	647/Cy5	anti-MITF	MITF	Abcam	ab12039	C5	anti-Mouse (Alexa 647)
2	488/FITC	Ki67-488	Ki67	CST	11882	D3B5	Alexa Fluor 488
2	555/Cy3	CD4-e570	CD4	eBioscience	41-2444-80	N1UG0	eFluor 570
2	647/Cy5	NGFR-647	NGFR	Abcam	AB195180	EP1039Y	Alexa Fluor 647
3	488/FITC	pERK-488	pERK	CST	4344	D13.14.4E	Alexa Fluor 488
3	555/Cy3	pRB-555	pRB	CST	8957	D20B12	Alexa Fluor 555
3	647/Cy5	CD45-647	CD45	BioLegend	304056	H130	Alexa Fluor 647
4	488/FITC	PD1-488	PD1	CST	15131	n/d	Alexa Fluor 488
4	555/Cy3	CD4-e570	CD4	eBioscience	41-2444-80	N1UG0	eFluor 570
4	647/Cy5	PDL1-647	PDL1	CST	15005	E1L3N	Alexa Fluor 647
5	488/FITC	EpCAM-488	EpCAM	CST	5198	VU1D9	Alexa Fluor 488
5	555/Cy3	Foxp3-570	FOXP3	eBioscience	41-4777-80	236A/E7	eFluor 570
5	647/Cy5	CD3-APC	CD3	eBioscience	17-0038-41	UCHT1	APC
6	488/FITC	pS6_240-488	pS6(240/244)	CST	5018	D68F8	Alexa Fluor 488
6	555/Cy3	CD45R-e570	CD45R	eBioscience	41-0452-80	RA3-6B2	eFluor 570
6	647/Cy5	CD45-647	CD45	BioLegend	304020	n/d	Alexa Fluor 647
7	488/FITC	Ecad-488	Ecad	CST	3199	24E10	Alexa Fluor 488
7	555/Cy3	Keratin-555	Keratin	CST	3478	C11	Alexa Fluor 555
7	647/Cy5	Vimentin-647	Vimentin	BioLegend	677807	O91D3	Alexa Fluor 647
8	488/FITC	EGFR-488	EGFR	CST	5616	D38B1	Alexa Fluor 488
8	555/Cy3	VEGFR2-555	VEGFR2	CST	12872	D5B1	Alexa Fluor 555
8	647/Cy5	gH2ax-647	gH2ax	BioLegend	613407	2F3	Alexa Fluor 647
9	488/FITC	Bax-488	Bax	BioLegend	633603	2D2	Alexa Fluor 488
9	555/Cy3	MAP-570	MAP2	eBioscience	41-9763-80	AP20	eFluor 570
9	647/Cy5	Bcl2-647	Bcl2	BioLegend	658705	100	Alexa Fluor 647
10	488/FITC	Mitotracker	n/d	Invitrogen	M7514	n/d	N/A
10	555/Cy3	ActinRed	n/d	Invitrogen	R37112	n/d	Alexa Fluor 555
10	647/Cy5	HCSred	n/d	Invitrogen	H32714	n/d	N/A